Available online at www.sciencedirect.com

ScienceDirect

Geochimica et Cosmochimica Acta 293 (2021) 103–126

Geochimica et Cosmochimica Acta

www.elsevier.com/locate/gca

New constraints from ^{26}Al-^{26}Mg chronology of anorthite bearing chondrules in unequilibrated ordinary chondrites

Guillaume Siron [a,*], Kohei Fukuda [a], Makoto Kimura [b], Noriko T. Kita [a]

[a] WiscSIMS, Department of Geoscience, University of Wisconsin-Madison, Madison, WI 53706, USA
[b] National Institute of Polar Research, Meteorite Research Center, Midoricho 10-3, Tachikawa, Tokyo 190-8518, Japan

Received 15 May 2020; accepted in revised form 21 October 2020; available online 1 November 2020

Abstract

^{26}Al-^{26}Mg ages were determined for 14 anorthite-bearing chondrules from five different unequilibrated ordinary chondrites (UOCs) with low petrologic subtypes (3.00–3.05). In addition, oxygen three isotopes of these chondrules were also measured. The selected chondrules are highly depleted in alkali elements, and anorthite is the only mesostasis phase, though they show a range of mafic mineral compositions (Mg# 76–97 mole%) that are representative of chondrules in UOCs. The mean Δ^{17}O values in these chondrules range from -0.44 ± 0.23‰ to 0.49 ± 0.15‰, in good agreement with previous studies of plagioclase-bearing chondrules from UOCs. Anorthite in all chondrules exhibit resolvable excess ^{26}Mg (>1.0 ± 0.4‰). Their inferred $(^{27}Al/^{26}Al)_0$ range from $(6.3 \pm 0.7) \times 10^{-6}$ to $(8.9 \pm 0.3) \times 10^{-6}$ corresponding to a timescale for chondrule formation of 1.8 ± 0.04 Ma to $2.16 \pm {}^{0.12}/_{0.11}$ Ma after CAIs using a canonical $(^{27}Al/^{26}Al)_0$ value of 5.25×10^{-5}. The ages from six chondrules in LL chondrites are restricted to between 1.8 Ma and 1.9 Ma, whereas eight chondrules in L chondrites show ages from 1.8 Ma to 2.2 Ma, including three chondrules at ~2.0 Ma and two chondrules at ~2.15 Ma.

The inferred chondrule formation ages from this study are at the peak of those previously determined for UOC chondrules, though with much shorter durations. This is potentially due to the time difference between formation of anorthite-bearing chondrules and typical UOC chondrules with alkali-rich compositions. Alternatively, younger chondrules ages in previous studies could have been the result of disturbance to the Al-Mg system in glassy mesostasis even at the low degree of thermal metamorphism in the parent bodies. Nevertheless, the high precision ages from this study (with uncertainties from 0.04 Ma to 0.15 Ma) indicate that there was potentially more than one chondrule forming event represented in the studied population. Considering data from LL chondrites only, the restricted duration (≤0.1 Ma) of chondrule formation ages suggests an origin in high density environments that subsequently lead to parent body formation. However, the unusually low alkali contents of the studied chondrules compared to common alkali-rich chondrules could also represent earlier chondrule formation events under relatively lower dust densities in the disk. Major chondrule forming events for UOCs might have postdated or concurrent with the younger anorthite-bearing chondrule formation at 2.15 Ma after CAIs, which are very close to the timing of accretion of ordinary chondrite parent bodies that are expected from thermal evolution of ordinary chondrite parent bodies.

Keywords: ^{26}Al-^{26}Mg chronology; Chondrule formation ages; SIMS; UOCs; Initial ^{26}Al/^{27} Al; Anorthite

1. INTRODUCTION

Chondrules, one of the main components of chondrites, represent solidified melt droplets resulting from transient high temperature heating of dust aggregates in the protoplanetary disk (Grossman, 1988; Jones, 2012).

* Corresponding author.
E-mail address: siron@wisc.edu (G. Siron).

https://doi.org/10.1016/j.gca.2020.10.025
0016-7037/

Shock-wave heating is the most developed model of chondrule formation, though the detailed mechanisms of chondrule formation has been a controversial subject for decades (Desch et al., 2012). The timing and duration of chondrule formation are the keys to constrain the mechanism(s) of chondrule formation and help us to understand the evolution of the early Solar System. Indeed, studies suggest that chondrules in ordinary chondrites (OCs), which would have formed under high dust density disk environments, should show a very short period of formation ages (i.e., <0.1 Ma) due to subsequent planetesimal formation (Alexander, 2005; Alexander et al., 2008; Alexander and Ebel, 2012). Such short timescales would prevent any large-scale mixing of materials in the protoplanetary disk (Cuzzi et al., 2010). The two most commonly used chronometers for chondrule formation ages are the ^{207}Pb-^{206}Pb system (Connelly et al., 2012; Bollard et al., 2017) and the ^{26}Al-^{26}Mg system (Hutcheon and Hutchison, 1989; Hutcheon and Jones, 1995; Kita et al., 2000; Villeneuve et al., 2009; Kita and Ushikubo, 2012). In contrast to the prediction of a short time interval (0.1 Ma) for the formation of UOC chondrules (Alexander and Ebel, 2012), most studies indicate that UOC chondrule formation occurred 0–4 Ma and 1.5–3 Ma after Ca, Al-rich inclusions (CAIs) for Pb-Pb and Al-Mg ages, respectively (e.g., Bollard et al., 2017; Pape et al., 2019). It is important to note that the ages obtained from these two methods represent the timing for their last melting event (Kita and Ushikubo, 2012; Bollard et al., 2017, 2019).

The ^{26}Al-^{26}Mg system applied to chondrule chronology is a powerful tool because of its short half-life (7.05×10^5 years after Nishiizumi, 2004). This allows for the precise determination of ages within a few million years of the formation of the oldest solids in the Solar System, CAIs (Kita et al., 2013). Due to the relatively low initial ratio of $(^{26}Al/^{27}Al)_0$ in chondrules ($\leq 10^{-5}$) compared to CAIs (5×10^{-5}), earlier in-situ secondary ion mass spectrometry (SIMS) analyses were conducted on Al-rich chondrules (Hutcheon and Jones, 1995; Russell et al., 1996, 1997) and one "clast chondrule" that contain coarse anorthite (Hutcheon and Hutchison, 1989). More recently, several studies have constrained the ^{26}Al-^{26}Mg ages of ferromagnesian chondrules in unequilibrated ordinary chondrites (UOCs), either using high primary current (Villeneuve et al., 2009; Pape et al., 2019) or a smaller spot size (Kita et al., 2000; Mostefaoui et al., 2002; Rudraswami and Goswami, 2007; Rudraswami et al., 2008; Bollard et al., 2019). The higher count rates obtained by the first method allows the use of high precision multi-collection Faraday cup (MCFC) analyses. This works well for many UOC chondrules because most contain glassy mesostasis with low ^{27}Al/^{24}Mg ratios and relatively small excesses in ^{26}Mg. On the other hand, analyses using a small spot size can avoid beam overlap between high-Ca pyroxene and mesostasis, and also make it possible to target phases with high ^{27}Al/^{24}Mg ratios that have larger excess ^{26}Mg. These analyses can provide important constrains despite the lower precision associated with lower counts for Mg isotopes. Results from these two different approaches give significantly different durations for chondrule formation. The first approach yields a long duration ~1.5 Ma over which chondrule formation occurred, a range that is greater than analytical uncertainties for each chondrule age (Villeneuve et al., 2009; Pape et al., 2019), whereas the second indicates a more restricted duration ~0.4 Ma that is comparable to the uncertainties on individual chondrule ages (Kita et al., 2000). Alexander and Ebel (2012) suggested that UOC chondrules would have a limited range of formation ages and proposed that the larger range observed by Villeneuve et al. (2009) may represent the disturbance of the Al-Mg system due to parent body metamorphism and/or result from mixed analyses between mesostasis and high-Ca pyroxene. The SIMS Al-Mg analyses using large analytical spots that overlap high Al/Mg mesostasis (glass and plagioclase) and mafic minerals would produce mixing line in the isochron diagram, which would not allow for the assessment of a possible disturbance of the isochron.

This paper aims to establish the true range of OC chondrule formation ages and constrain the formation mechanism of chondrules in OCs. In order to eliminate the potential disturbance of the Al-Mg system, we selected coarse-grained anorthite-bearing chondrules from several L/LL 3.00–3.05 UOCs for Al-Mg analyses, though anorthite-bearing chondrules are uncommon in UOCs (Kita et al., 2000, 2010). Experimental data for Mg self-diffusion in anorthite indicates that the Al-Mg system in anorthite should not be disturbed in the subtypes 3.00–3.05 UOCs that have experienced limited degrees of metamorphism (Van Orman et al., 2014). In order to obtain reliable SIMS data, we restricted the primary beam size so that analyses did not overlap adjacent phases as in our previous study (Kita et al., 2000).

These analyses were performed with our upgraded primary radiofrequency (RF) oxygen plasma ion source that allows us to use smaller and denser primary beams for Al-Mg isotope analyses (Hertwig et al., 2019). Furthermore, modifications of the detection system for lower Mg secondary ion intensities ($\leq 10^6$ cps) significantly improve the analytical precision by: (1) reduction of MCFC thermal noise by using high gain feedback resistor (10^{12} ohm; Fukuda et al., 2020a, 2020b) and (2) improvements in counting statistics by using multi-collector electron multiplier (MCEM) pulse counting system (Kita et al., 2018; Hertwig et al., 2019).

2. METHODS

2.1. Samples

The UOCs selected for this study have all been classified as subtypes 3.00–3.05 from their Cr_2O_3 contents in fayalitic olivine (Grossman and Brearley, 2005). The sections studied here are as follows; Semarkona (LL3.00) polished thin section (PTS) USNM 1805-9, polished mounts of NWA 8276 (L3.00) and NWA 8649 (LL3.05) from University of New Mexico, and QUE 97008 (L3.05) PTS #12 and MET 00452 (L/LL 3.05) PTS #16 from US Antarctic meteorite program (ANSMET). Classification of MET 00452 is from its pair MET 00526 (L/LL3.05; Grossman and Brearley, 2005). Semarkona was classified as LL3.01 based on

Fe-Ni metal (Kimura et al., 2008) that is sensitive to low degree thermal metamorphism between 3.00 and 3.10. According to Fe-Ni metal observations (Kita et al., 2019), NWA 8276 seems to be slightly more metamorphosed than Semarkona and similar to other 3.05 UOCs studied here. Semarkona has low shock stage S2, and MET 00452, MET 00526, QUE 97008, and NWA 8649 were described as low shock. No information for shock stage is known for a paired meteorites NWA 7731 and NWA8276, though we do not recognize any obvious shock features.

2.2. Electron microscopy

Backscattered secondary electron (BSE) and secondary electron (SE) images were acquired using a Hitachi 3400 variable pressure scanning electron microscope (SEM). More than 800 chondrules from multiple UOC sections were examined using EDS spectra and BSE images in order to search chondrules that contain coarse grained anorthite (≥10 μm) large enough to analyze with the 6 μm SIMS spot.

Major and minor element analyses were obtained using electron probe microanalyzers (EPMA) at the Eugene Cameron Electron Microprobe Laboratory of the University of Wisconsin-Madison using 15 kV and 15 nA beam conditions. Plagioclase analyses were obtained during three different sessions. The first and 3rd sessions used the Cameca SX5 Field Emission gun microprobe using a beam size of 3 μm, the 2nd session used the Cameca SX51 microprobe with a beam size of 5 μm, both are equipped with five wavelength dispersive spectrometers. Counting times were 10 seconds on the wavelength peak and 5 seconds on both backgrounds, except for the second session where Al and Ti were measured using the mean atomic number (MAN) method (Donovan et al., 2016), for which no background is required. During this second session, counting times were reduced for Na, K and Mn to 5 seconds on both backgrounds and peak and increased to 20 (peak) and 10 (backgrounds) seconds for Mg. Albite for Na and Si, anorthite for Ca and Al, microcline for K, hematite (1st session) or BHVO glass (2nd and 3rd session) for Fe, forsterite (1st session) or andesite glass (2nd and 3rd sessions) for Mg, Cr_2O_3 oxide for Cr, Mn-olivine for Mn and TiO_2 oxide for Ti served as standards. Olivine and pyroxenes were analyzed using a 3 μm beam size. The same counting times as in the third session of plagioclase analyses were used. The following standards were used for olivine: Mg-olivine (Mg, Si), augite (Ca), anorthite (Al), hematite (Fe), Cr_2O_3 oxide (Cr), Mn-olivine (Mn) and TiO_2 oxide (Ti). The following standards were used for pyroxenes: enstatite (Mg, Si), augite (Ca), anorthite (Al), hematite (Fe), Cr_2O_3 oxide (Cr), Mn-olivine (Mn) and TiO_2 oxide (Ti). All elements were far above detection limits, except TiO_2 and Na_2O that had detection limits of 0.030 wt.% and 0.015 wt.%, respectively.

No differences were found between glass and mineral standards for major and trace elements between the different sessions. Notably, MgO contents were between 0.5–1 wt.% for pure anorthite (i.e., > An_{93} in this study; where An = Ca/(Ca + Na + K) mol%). The data were reduced using the Probe software package using both ZAF and ϕρz matrix correction routines. In this paper, all uncertainties for major and minor elements are one standard deviation (1SD).

2.2.1. Plagioclase end-member determination

Anorthite-rich plagioclase in chondrules from the least metamorphosed chondrites typically contain high MgO (0.5–1%; Kita et al., 2000; Kurahashi et al., 2008), distinctly higher than from what is found in terrestrial and extraterrestrial igneous rocks. The most striking differences are their high MgO, FeO, and MnO contents, that can reach up to ~2 wt.% combined (MacPherson and Huss, 2005). These high contents of divalent cations can be incorporated into the plagioclase structure by two different substitutions:

$$\mathrm{Ca} \rightarrow (\mathrm{Mg,Fe,Mn}) \quad (1)$$

$$2\mathrm{Al} \rightarrow (\mathrm{Mg,Fe,Mn})+\mathrm{Si} \quad (2)$$

It is unclear whether these divalent cations enter the plagioclase structure with one or the other substitutions and it seems to depend on the samples analyzed (Beaty and Albee, 1980). Nevertheless, there seems to be a preference for substitution (2) to explain the incorporation of Fe, Mg and Mn cations. This is especially well delineated in lunar samples (Wenk and Wilde, 1973; Longhi et al., 1976; Beaty and Albee, 1980).

Additionally, it has been documented that plagioclase grains from extraterrestrial samples exhibit excess structural silica ($\square Si_4O_8$), especially in lunar samples (Weil et al., 1970; Wenk and Wilde, 1973; Bruno and Facchinelli, 1975; Beaty and Albee, 1980; Anon, 2014), but also recently in plagioclase bearing chondrules in CR and Acfer 094 (Tenner et al., 2019) and in Pasamonte eucrite (Mittlefehldt and Berger, 2017). The incorporation of excess silica follows two substitution from albite and anorthite endmember:

$$\mathrm{Na} + \mathrm{Al} \rightarrow \mathrm{Si} + \square \quad (3)$$

$$\mathrm{Ca} + 2\mathrm{Al} \rightarrow 2\mathrm{Si} + \square \quad (4)$$

The proportion of the different plagioclase endmembers are computed using linear algebra, as described in Thompson (1982) and Spear, Rumble and Ferry (1982):

$$Ax = b \quad (5)$$

where A represents the matrix for the stoichiometry of each endmember, with rows representing the stoichiometry for each element of the endmembers (vectors), x is the vector of the different proportions of endmembers and b is the measured contents for each cation. Taking into account all possible endmember, it takes the form of:

$$\begin{bmatrix} 0 & 1 & 0 & 0 & 0 & 0 & 0 & 0 & 0 & 0 \\ 1 & 0 & 0 & 0 & 0 & 0 & 1 & 1 & 1 & 0 \\ 0 & 0 & 1 & 0 & 0 & 0 & 0 & 0 & 0 & 0 \\ 1 & 0 & 0 & 1 & 0 & 0 & 1 & 0 & 0 & 0 \\ 0 & 0 & 0 & 0 & 1 & 0 & 0 & 1 & 0 & 0 \\ 0 & 0 & 0 & 0 & 0 & 1 & 0 & 0 & 1 & 0 \\ 2 & 1 & 1 & 2 & 2 & 2 & 0 & 0 & 0 & 0 \\ 2 & 3 & 3 & 2 & 2 & 2 & 3 & 3 & 3 & 4 \end{bmatrix} \cdot \begin{bmatrix} CaAl_2Si_2O_8 \\ NaAlSi_3O_8 \\ KAlSi_3O_8 \\ CaAl_2Si_2O_8 \\ MgAl_2Si_2O_8 \\ FeAl_2Si_2O_8 \\ MnAl_2Si_2O_8 \\ CaMgSi_3O_8 \\ CaFeSi_3O_8 \\ CaMnSi_3O_8 \\ [\,]Si_4O_8 \end{bmatrix} = \begin{bmatrix} Na \\ Ca \\ K \\ Mg \\ Fe \\ Mn \\ Al \\ Si \end{bmatrix} \quad (6)$$

The coefficients for the different proportions of the endmembers is computed using non-negative least square fitting, with the target variable being the measured cations. In general, the results of this method have been in agreement with the previously used method from Beaty and Albee (1980). This method has the advantage of forbidding any negative values for endmembers, which would result in the overestimation of the other endmembers. It is especially true when plagioclases have low $\square$ Si_4O_8 and (Mg,Fe,Mn) $Al_2Si_2O_8$ compositions. It can be applied for low Ti and Cr content plagioclases since it does not take into account these two cations.

2.3. SIMS oxygen three isotopes analyses

Oxygen three isotope measurements were conducted in a single session using the IMS1280 at the WiscSIMS laboratory of the University of Wisconsin-Madison. Analytical conditions are similar to those described in Kita et al. (2010) and use MCFC for the three isotopes. A focused gaussian Cs^+ primary beam at ~2 nA was used in order to achieve counts per second (cps) in the range of (2–3) × 10^9 for $^{16}O^-$, the spot size was about 12 × 10 μm in diameter. A mass resolving power (MRP) of ~5000 was achieved in order to separate the isobaric interference of $^{16}O^1H$ to ^{17}O. The ^{17}O isotope signal was measured using a Faraday cup (FC) detector with a 10^{12} Ω resistance for improved precision. The ^{16}O and ^{18}O isotope signals were measured with FC detectors of 10^{10} and 10^{11} Ω, respectively. Additionally, $^{16}O^1H$ was measured at the end of each measurement to estimate potential tailing effect on ^{17}O counts. As in the previous studies, 12–16 unknown chondrule analyses are bracketed by 8 analyses of SC-Ol standard (e.g., Hertwig et al., 2018). A slight drift for both $\delta^{18}O$ and $\delta^{17}O$ standard data (EA1) was recognized during this session, which should be carefully treated for UOC chondrule data where variabilities in $\Delta^{17}O$ are relatively small (≤1‰; Kita et al., 2010). Thus, we applied a drift correction to the entire dataset using repeated analyses of the SC-Ol running standard, instead of a simple correction by a set bracket standard analyses (e.g., Kita et al., 2010). In order to correct the drift during the entire 54 h of the analyses, we divided the session into three sections based on the evolution of SC-Ol data with time (see, EA1). The first section did not require a drift correction, while the second section required using a 3rd order polynomial fit for both $\delta^{18}O$ and $\delta^{17}O$ and the last section required a 2nd order polynomial fit for $\delta^{18}O$ and a linear fit for $\delta^{17}O$. P-values of each coefficient were checked to achieve a good fit (EA1). The reproducibilities of the SC-Ol standard measurements were typically 0.2‰ for $\delta^{18}O$, 0.25‰ for $\delta^{17}O$ and 0.25‰ for $\Delta^{17}O$, after drift correction.

Five additional olivine standards (from Fo_{60} to Fo_{100}), three low-Ca pyroxene standards (Mg# 0.7–0.97) and one diopside standard (Kita et al., 2010; Fukuda et al., 2020a, 2020b) were analyzed at the beginning of the session to correct matrix effects depending on the mineral compositions. In this analysis session, the instrumental biases among olivine standards were nearly the same (≤±0.3‰) within the range of compositions (EA1), so that no additional bias correction depending on Fo contents was applied. We typically find 0.5-1‰ changes among these olivine standards (e.g., Tenner et al., 2015), which may change depending on primary beam conditions. This finding is not surprising since many studies have demonstrated that most of the matrix effect for the olivine solid solution occur in Fe-rich compositions below Fo_{50} (Valley and Kita, 2009; Isa et al., 2017). Similarly, no significant matrix effect was found for low-Ca pyroxenes standards for such a limited range of Mg# (70–97 mole%). Correction of matrix effects for Ca content was achieved using the diopside standard. Additionally, one anorthite standard was used to correct for instrumental bias for plagioclases analyses.

This session showed a small mass dependent fractionation within individual analyses so instead of using the 2SE we use the 2SD of standard bracket measurements for unknown analyses. Uncertainties for each individual analysis were estimated by propagating the 2SD of the standard measurements bracketing the analysis, the 2SE of these standard analyses, the uncertainty on the fit (95% confidence interval) when corrected for drift and an additional factor of 0.3‰ to account for the error on the reference values for standards from laser fluorination. The host chondrule O isotopic compositions were computed following the procedure established in Ushikubo et al. (2012) and Tenner et al. (2013). During this session, the 3SD for $\Delta^{17}O$ of the SC-Ol of all measurements was 0.43‰. In a first step, a mean $\Delta^{17}O$ value, including all the analyses for a chondrule, was computed and analyses that are outside of 3SD (0.43‰) from the mean were identified. Data were rejected if the remainder of the analyses were all within 3SD limit of their mean value. The remaining analyses are used to compute the mean oxygen isotope ratios (for $\delta^{18}O$, $\delta^{17}O$, and $\Delta^{17}O$), which were assumed to be those of host chondrules. Anorthite analyses were not used to compute host chondrule compositions. Similarly to individual analyses, the uncertainty on the host chondrule composition for each chondrule is the propagation of 2SE of all individual measurements inside one chondrule, along with the additional uncertainties in the instrumental mass fractionation; 0.3‰ and 0.15‰, for $\delta^{18}O$ and $\delta^{17}O$, respectively (Kita et al., 2010).

2.4. SIMS Al-Mg isotopes analyses

All Al-Mg isotope measurements were conducted using the IMS 1280 at the WiscSIMS Laboratory of the University of Wisconsin-Madison. The conditions for the analyses were similar to those in previous studies (Kita et al., 2012; Hertwig et al., 2019; Fukuda et al., 2020a, 2020b). Primary ions of O_2^- were focused in Gaussian mode with a 23 kV impact energy (−13 kV at the ion source and +10 kV at the sample surface) from the new RF ion source. Transfer optics were tuned using a Max Area of 40 μm (magnification 200×). Entrance slits were set to 90 μm and exit slits to 500 μm, which provide a MRP of ~2200 (M/ΔM). Although this MRP setting is lower than that required for separating Mg hydride interferences, Hertwig et al. (2019) confirmed that interferences from hydride and $^{48}Ca^{2+}$ are sufficiently small compared to Mg^+ signals, i.e., less than 0.1‰.

Delta notation δ^{25}Mg and δ^{26}Mg used absolute Mg isotope ratios to normalize raw data as follows; (^{25}Mg/^{24}Mg) = 0.12663 and (^{26}Mg/^{24}Mg) = 0.13932 (Catanzaro et al., 1966). Instrumental bias was corrected using several standards matching the compositions of measured olivine, pyroxenes and plagioclase. The excess ^{26}Mg after mass fractionation correction (δ^{26}Mg*) was calculated using an exponential law in two steps, similarly to the approach of Hertwig et al. (2019) and as follows:

$$\delta^{26}Mg^{*} = \left[\left(1+\frac{\delta^{26}Mg}{1000}\right) - \left(1+\frac{\delta^{25}Mg}{1000}\right)^{\left(\frac{1}{\beta}\right)}\right] \times 1000 \quad (7)$$

$$\delta^{26}Mg^{*} = \Delta^{26}Mg \times \left(1+\frac{\delta^{25}Mg}{1000}\right)^{\left(\frac{1}{\beta}\right)} \quad (8)$$

The exponential parameter β was assumed to be 0.5128 (Davis et al., 2015) for plagioclases analyses and determined from olivine standards for olivine and pyroxene analyses. The δ^{26}Mg* is equivalent to Δ^{26}Mg when the natural mass dependent fractionation measured as δ^{25}Mg equals zero (Ushikubo et al., 2017). Following the procedure of Tenner et al. (2019), we assume chondrules do not have a significant natural mass dependent fractionation in δ^{25}Mg (~0‰) and estimated δ^{26}Mg* to be the same as Δ^{26}Mg.

For anorthite measurements, the relative sensitivity factors of standards were used to correct for instrumental bias as follows:

$$RSF = \frac{\left(\frac{^{27}Al}{^{24}Mg}\right)^{SIMS}_{measured}}{\left(\frac{^{27}Al}{^{24}Mg}\right)^{EPMA}_{reference}} \quad (9)$$

Three different analytical settings were used, two for anorthite measurements with 6 μm and 15 μm spot sizes, and one for olivine and pyroxenes with a 8 μm spot size. In all sessions, three Mg isotopes and $^{27}Al^{+}$ signals were detected simultaneously on the multicollection (MC) system. In all conditions, the major isotopes $^{24}Mg^{+}$ and $^{27}Al^{+}$ were detected on FCs. Minor isotopes $^{25}Mg^{+}$ and $^{26}Mg^{+}$ were measured on FCs for olivine/pyroxene and large spot anorthite analyses, while during small spot analyses they were detected using electron multipliers (EM) on multicollector arrays (Hamamatsu EM).

2.4.1. MC FC-EM analyses of anorthite (6 μm spot size)

Since most of the chondrules had smaller plagioclases grains (<10 μm), two sessions were conducted using a small spot size of ~6 μm. The primary intensity was ~160 pA, resulting in secondary $^{24}Mg^{+}$ and $^{27}Al^{+}$ intensities of (6–8) × 10^{5} cps and ~2 × 10^{7} cps for anorthite glass standard with 1.0 wt% MgO. FC amplifier boards with 10^{12} Ω and 10^{11} Ω resistances were used for detecting $^{24}Mg^{+}$ and $^{27}Al^{+}$, respectively. Secondary $^{25}Mg^{+}$ and $^{26}Mg^{+}$ isotope signals were 7 × 10^{4} cps to 1 × 10^{5} cps that were detected using EMs. Analyses typically consisted of 120 s of presputtering followed by centering of secondary deflectors and 400 cycles of data acquisitions with 4 s counting time. The FC baseline was measured for $^{24}Mg^{+}$ during presputtering and the baseline average of 8 analyses was taken as the value to correct $^{24}Mg^{+}$ intensities. The variabilities of the baseline were typically ~150–180 cps (1SD). The overall analysis time was ~32 min. In order to maintain constant EM gains, relative to the FC detectors, the high voltage (HV) of each EM was adjusted at the 20th and 220th cycles using a Cameca software routine. The gain drift for each EM was monitored and corrected using a second discriminator connected parallel to the first one (Kita et al., 2019, see detailed information in EA2).

Two anorthite composition glass standards with MgO contents of 0.6 wt.% and 1 wt.% (Kita et al., 2012) were used to correct for RSF and δ^{26}Mg*, which are in the same range of MgO contents with those of the unknown plagioclase grains in the chondrules. Internal errors were typically 0.4–0.6‰ (2SE) for Δ^{26}Mg and 0.5–1% for ^{27}Al/^{24}Mg ratios. Within several hours of continuous analyses, repeated analyses of anorthite glass standard were reproducible to nearly within their internal errors. However, because of relatively high intensities applied to the EMs (~10^{5} cps), the measured Mg isotope ratios of the standard drifted over the entire analysis sessions. The first session was corrected for a 6‰ drift of the Δ^{26}Mg values during the entire session of five days, using a weighted least square algorithm for each day of analysis (EA3). The second session did not require any drift correction in-between mass calibrations, which represent approximately one day of analyses. As for the O isotope analyses, the p-value of each coefficient were checked to determined which was the best polynomial order to use for the drift correction. The reproducibility for standard analyses after drift correction was typically 0.4–0.7‰ (2SD) for Δ^{26}Mg. Some analyses that touched a high-Ca pyroxene were stopped before the end of the 400 cycles. For such analyses, only the cycles before the abrupt increase of Mg^{+} were taken to calculate the Δ^{26}Mg and ^{27}Al/^{24}Mg ratios and the standard analyses used for calibrating δ^{26}Mg* were also recalculated using the same number of cycles in order to account for the change in ^{27}Al/^{24}Mg and a potential bias in Δ^{26}Mg with the depth of analysis (Hertwig et al., 2019). Final uncertainties for δ^{26}Mg* represent the propagation of internal errors (2SE), errors in the fit for the drift correction at the time of the analysis (95% confidence interval) and the 2SE of the standard measurements. This uncertainty is dominated by the internal error. The uncertainties for the ^{27}Al/^{24}Mg ratios represents the propagation of internal errors (2SE) and the 2SE of the standard measurements. Again, this uncertainty is dominated by the internal error. Two brackets of standards behaved significantly differently during the middle of the second session (red section in EA3, spreadsheet "07-23-2019").

2.4.2. MCFC analyses of anorthite (15 μm spot size)

An O_2^{-} primary intensity of 4nA resulted in secondary $^{24}Mg^{+}$ and $^{27}Al^{+}$ intensities of ~2 × 10^{7} cps and ~5 × 10^{8} cps for the anorthite glass standard with 1.0 wt % MgO. FC detectors were used for all three Mg isotope signals with 10^{12} Ω resistances and $^{27}Al^{+}$ with 10^{11} Ω resistance. The analyses consisted of 100 sec of presputtering, followed by the alignment of secondary deflectors and

20 cycles of data acquisitions with 10 s counting time for each cycle. The overall analysis time was ~8 min. As in the FC-EM sessions, two glass standards (0.6 wt.% and 1 wt.% of MgO) were used to correct for instrumental bias. For Δ^{26}Mg, internal errors were typically 0.2–0.45‰ (2SE), and the reproducibility for the 34 standard measurements of the session was 0.38‰ (2SD). A slight linear drift correction was required for the entire session that lasted ~6 h because we started the analyses within several hours of switching the FC amplifier boards. The ^{27}Al/^{24}Mg ratios had internal errors of 0.15–0.2% and a reproducibility for the 34 standard measurements of 0.25% (2SD). The errors in the ^{27}Al/^{24}Mg ratios were propagated the same way as for FC-EM data.

2.4.3. MCFC analyses of olivine and pyroxenes (8 μm spot size)

A 1 nA O_2^- focused primary beam resulted in the secondary $^{24}Mg^+$ intensity of $\sim 2 \times 10^8$ cps for olivine and pyroxene that was measured with a FC detector with a 10^{10} Ω resistor. The masses $^{25}Mg^+$, $^{26}Mg^+$ and $^{27}Al^+$ were measured using FC detectors with 10^{11} Ω resistors. Counting times were the same as for the MCFC analyses of anorthite. Fifteen different olivine standards (Fo_{60}-Fo_{100}) and five pyroxene standards (two diopside and three low-Ca pyroxenes with Mg# 85–96 mole%) were measured to correct for natural and instrumental bias (Fukuda et al., 2020a, 2020b). With such a large number of standards the exponential factor β was determined using olivine standards by fitting the data in a $\delta^{26}Mg'$ vs $\delta^{25}Mg'$ diagram, with $\delta^{26\text{-}25}Mg' = 1000 \times \ln\{(\delta^{26\text{-}25}Mg + 1000)/1000\}$, resulting in a nominal value of 0.5169 (EA3 spreadsheet "d25Mg vs d26Mg" and EA4). This nominal value was obtained using only terrestrial olivine standards since extraterrestrial olivine standard might have very small variabilities in Δ^{26}Mg. Olivine Δ^{26}Mg values exhibited a small offset of 0.019 ± 0.010‰ (2SE) and pyroxene Δ^{26}Mg values were higher by 0.15 ± 0.025‰ (2SE) relative to the San Carlos olivine (SC-Ol) standard (EA4). Such offset between olivine and pyroxene might be due to small degree of mass independent fractionation within the SIMS instrument, which seem to occur in our analyses using finely focused intense primary beam conditions. This would not be fully evaluated in previous studies which used a smaller number of olivine and low-Ca pyroxene standards (typically only 2 for each in contrast to 15 olivine and 5 pyroxene standards in this study), but include several glass standards to estimate instrumental fractionation law.

Since terrestrial olivine does not exhibit any natural excess ^{26}Mg, no additional correction was required for these standards. Standards of meteoritic origin were corrected by their known $\delta^{26}Mg^*$, i.e. 0.0082 ± 0.0011‰ for KN-Ol (Kenna olivine; Larsen et al., 2011), 0.0085 ± 0.0018‰ for SW-Ol (Springwater olivine; Larsen et al., 2016). The natural excess ^{26}Mg of one meteoritic olivine standard was unknown (WN-Ol, Winona olivine), and was not used to correct the Δ^{26}Mg values. Additionally, the most Fe-rich standard (Fo_{59}) was not used since it was well below the Fo range of olivine unknowns of this study. Δ^{26}Mg values during the session were corrected for drift by dividing it into three sections in which simple linear corrections were possible. Internal errors for Δ^{26}Mg were typically 0.04–0.07‰ for the olivine measurements, and slightly higher for the pyroxene analyses at 0.06–0.15‰ (2SE). The reproducibility of the standard measurements after drift correction was typically 0.04–0.06‰ (2SD) for SC-Ol standard. The error propagation was the same as used for anorthite measurements.

2.4.4. Isochron regression

Isochron regressions were computed using the online version of IsoplotR (Vermeesch, 2018) with the maximum likelihood option, i.e., Model 1 (York et al., 2004). Uncertainties on ^{27}Al/^{24}Mg used for the regression did not take into account the uncertainty on the reference value (from EPMA measurements) for anorthite standards. Since uncertainty of the slopes are larger than 1% for all studied chondrules, it would not change the final uncertainty of the isochron slopes. Weighted means were also computed using the IsoplotR software.

3. RESULTS

Fourteen chondrules from five different chondrites were investigated for O and Al-Mg isotopes in this study. Among them, four chondrules are from QUE 97008, four from NWA 8276, two from NWA 8649, two from Semarkona and two from MET 00452. Oxygen three isotopes, as well as Al-Mg isotopes, were obtained for all chondrules. One chondrule from Semarkona (c34) had been previously analyzed for Al-Mg isotopes and O three isotopes (CH23 in Kita et al., 2000; Kita et al., 2010, respectively). Nevertheless, due to the improved precision for both methods, it was analyzed with all other chondrules, except for the EPMA measurements of silicate minerals.

Full analyses for all phases are accessible in the supplementary materials. The EPMA analyses of olivine, pyroxenes and plagioclases are located in EA5. SIMS O isotopes data are in EA1 and Al-Mg isotopes analyses are in EA3. Pictures for all SIMS pits for both methods, as well as BSE images of the locations of these analyses inside each chondrule are provided in EA6.

3.1. Petrography of chondrules and mineral chemistry

Figs. 1 and 2 show all chondrules analyzed for Al-Mg and O isotopes. Tables 1–3 list the olivine, pyroxene and plagioclase compositions, respectively. The petrography and mineral chemistry of these chondrules are described below. Three out of the 14 selected chondrules were FeO-poor (Mg#>90), while the others are FeO-rich (Mg#<90) with a wide range of Mg# (76–90). Typical porphyritic chondrules are subdivided into types I and II according to Mg# >90 and <90, respectively, and into porphyritic olivine (PO), porphyritic olivine pyroxene (POP), and porphyritic pyroxene (PP) chondrules according to the modes of olivine and pyroxene phenocrysts; olivine volume % >80%, 20–80%, <20%, respectively, (Jones, 1994). Here, we adopt these classification schemes to anorthite-bearing chondrules studied here.

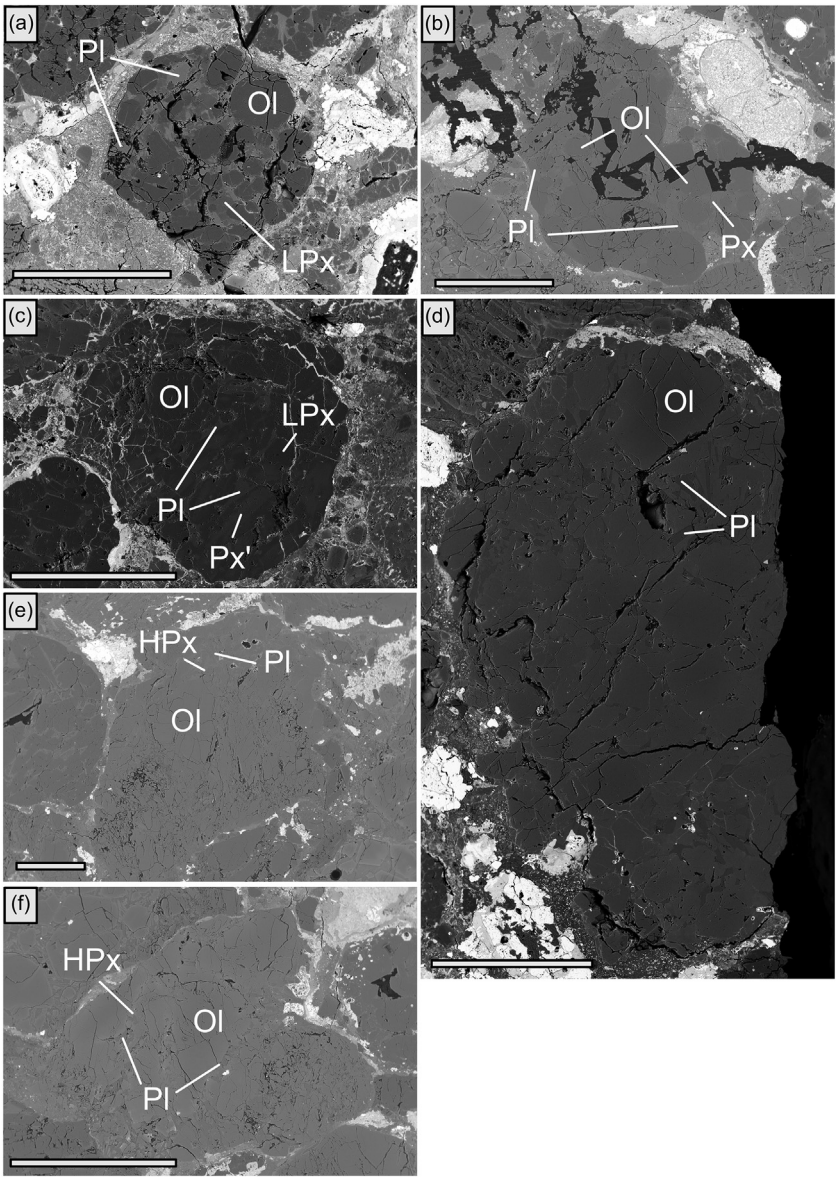

Fig. 1. BSE images of 6 different chondrules. (a) NWA8276 c69 (type I-POP), (b) QUE97008 c61 (type I-POP), (c) NWA8649 c17 (Type I-PP), (d) NWA8276 c7 (type II-PO), (e) QUE97008 c51 (type II-PO), f) QUE97008 c143 (type II-PO). Mineral abbreviations are as follows: olivine (Ol), low-Ca pyroxenes (LPx), high-Ca pyroxenes (HPx), pyroxenes with various amount of Ca (Px), plagioclase (Pl); Px′ for NWA 8649 c17 denotes pyroxene cores that are slightly enriched in Ca compare to low-Ca rims. Scale bar is 500 μm. See text for a more detailed description of the different phases and compositions.

3.1.1. Type I plagioclase-bearing chondrules

Two type-I POP chondrules, NWA 8276 c69 (Fig. 1a) and QUE 97008 c61 (Fig. 1b), show very similar textures and compositions for their olivine and pyroxene phenocrysts. Olivine phenocrysts are equant and have sizes ranging from 50 to 200 μm with homogenous compositions ($Fo_{95\text{-}97}$, see Table 1). There are no low-Ca pyroxenes, but the pyroxenes that are present have limited amounts of Ca with compositions of ($Wo_7En_{90}Fs_3$ for NWA8276 c69) and ($Wo_{13}En_{80}Fs_7$ for QUE97008 c61), respectively (Table 2). These pyroxenes are interstitial to the larger olivine phenocrysts. The remaining space is occupied by interstitial plagioclase grains with An_{99} in both chondrules (Table 3). Another type I chondrule is a PP chondrule, NWA 8649 c17 (Fig. 1c), which exhibits an inverse zoning in its pyroxene phenocrysts, with increase of Mg# toward the rims, from $Wo_3En_{85}Fs_{12}$ in the core to $Wo_3En_{90}Fs_7$ at the rims (see EA5). The boundaries between cores and rims are very sharp. Small high-Ca pyroxene overgrowths can be observed. Plagioclase is present as an interstitial phase with a composition of $\sim An_{94}$.

3.1.2. Type II plagioclase-bearing chondrules

Four type II chondrules can be grouped together by their similar textures, which include NWA 8276 c7 (Fig. 1d), QUE 97008 c51 (Fig. 1e) and c143 (Fig. 1f) and

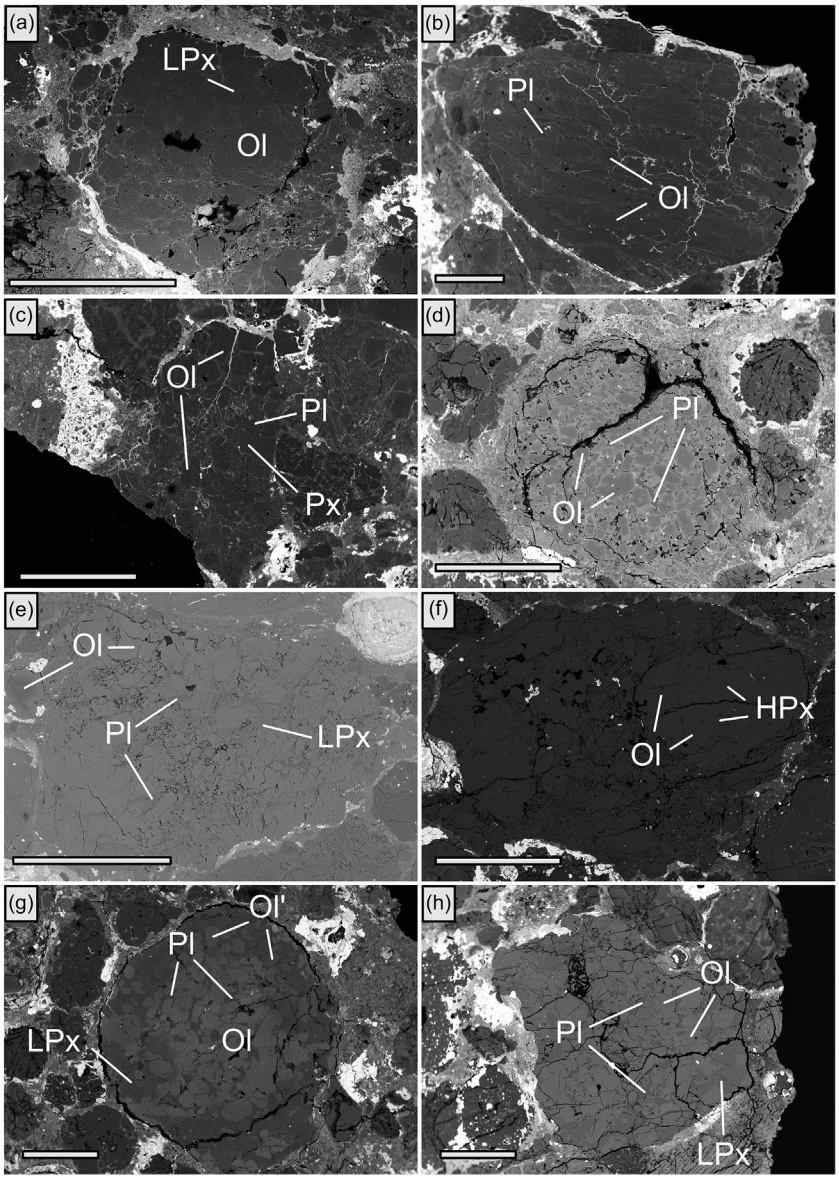

Fig. 2. BSE images of 8 different chondrules. (a) NWA8649 c87 (type II-PO), (b) MET00452 c19 (type II-PO), (c) MET00452 c111 (type II-POP), (d) NWA8276 c87 (type II-PO), (e) QUE97008 c150 (type II-PO), (f) Semarkona c47 (type II-PO), (g) NWA8276 c88 (type II-POP), (h) Semarkona c34 (type II-POP). Mineral abbreviations are the same as those in Fig. 1. Olivine inclusions in NWA8276 c88 is shown as (Ol′). Scale bar is 500 μm. See text for a more detailed description of the different phases and compositions.

NWA 8649 c87 (Fig. 2a). These chondrules can all be classified as type II-PO and have large olivine phenocrysts with only minor amounts of interstitial low-Ca pyroxenes that exhibit zoning toward more pigeonitic compositions, except for NWA 8276 c7 that does not have any low-Ca pyroxene. Plagioclase occurs as elongated laths, except for NWA 8649 c87 where the plagioclase grains are interstitial and not euhedral. Their Fo contents range between Fo_{85} and Fo_{90} (Table 1), while the Mg# of pyroxene phenocrysts are between 81 and 91 with low Ca content, $Wo_{4\text{-}5}$, except for NWA 8276 c7 with up to Wo_{11} (Table 2).

MET 00452 c19 is a very large type II-PO chondrule (2.5–3 mm) with barred olivine phenocrysts (Fig. 2b). The olivine phenocrysts are elongated in one direction and show a slight zonation toward the rims as can be seen in a BSE image (Fig. 2b). The cores of the olivine phenocrysts have compositions of Fo_{83} with a limited zoning toward the rims, which did not allow us to obtain a good EPMA measurement of the Fe-rich rim with a 3 μm spot size. The plagioclase grains are elongated at a high angle to the olivine orientation, with a 60° angle. The pyroxene grains ($Wo_3En_{86}Fs_{11}$) are interstitial to the plagioclase grains and the olivine phenocrysts. The plagioclase grains have a composition of $\sim An_{98}$.

MET 00452 c111 is a type II-POP chondrule (Fig. 2c). The olivine phenocrysts are large and euhedral with a homogeneous composition of $\sim Fo_{90}$. Subordinate pyroxene grains ($Wo_3En_{89}Fs_8$) occur between the larger olivine

Table 1
Average major and minor elements for olivine composition determined with EPMA.

	QUE 97008, 12				MET 00452, 16		NWA 8649		NWA 8276					Semarkona
	c51	c61	c143	c150	c19	c111	c17	c87	c7	c69	c87	c88 (core)	c88 (rim inc.)	c47
SiO_2	39.73	41.11	39.51	37.93	39.19	40.16	40.85	40.18	39.57	41.30	38.80	37.88	38.35	39.43
TiO_2	0.02	0.07	0.01	0.04	0.02	0.02	0.05	0.06	0.03	0.08	0.01	0.03	0.01	0.04
Al_2O_3	0.10	0.10	0.16	0.04	0.09	0.07	0.03	0.08	0.15	0.15	0.21	0.03	0.03	0.05
MgO	46.75	52.91	44.01	40.34	44.16	49.19	52.09	49.08	45.49	54.38	43.96	39.26	42.03	45.49
FeO	12.72	5.38	15.17	20.89	15.81	10.19	7.26	10.02	14.12	2.91	15.94	21.36	18.09	13.52
CaO	0.22	0.25	0.22	0.20	0.26	0.19	0.18	0.22	0.22	0.24	0.30	0.24	0.24	0.24
Na_2O	0.00	−0.01	0.03	−0.01	0.00	0.00	−0.02	−0.01	0.00	0.00	0.00	0.00	0.00	0.00
MnO	0.20	0.09	0.32	0.31	0.21	0.22	0.16	0.18	0.20	0.05	0.17	0.35	0.30	0.25
Cr_2O_3	0.61	0.55	0.55	0.29	0.61	0.52	0.30	0.59	0.56	0.59	0.45	0.49	0.47	0.56
Total	100.33	100.45	99.98	100.02	100.36	100.56	100.89	100.40	100.33	99.70	99.84	99.64	99.53	99.57
Si	0.989	0.988	1.00	0.984	0.990	0.986	0.984	0.987	0.991	0.989	0.985	0.990	0.988	0.990
Al	0.003	0.003	0.00	0.001	0.003	0.002	0.001	0.002	0.004	0.004	0.006	0.001	0.001	0.001
Mg	1.735	1.896	1.66	1.560	1.663	1.800	1.872	1.798	1.698	1.942	1.665	1.530	1.614	1.703
Fe	0.265	0.108	0.32	0.453	0.334	0.209	0.146	0.206	0.296	0.058	0.339	0.467	0.390	0.284
Ca	0.006	0.007	0.01	0.006	0.007	0.005	0.005	0.006	0.006	0.006	0.008	0.007	0.007	0.006
Mn	0.004	0.002	0.01	0.007	0.005	0.005	0.003	0.004	0.004	0.001	0.004	0.008	0.007	0.005
Cr	0.012	0.010	0.01	0.006	0.012	0.010	0.006	0.011	0.011	0.011	0.009	0.010	0.010	0.006
Sum Oct	2.022	2.022	2.00	2.032	2.021	2.029	2.031	2.025	2.016	2.018	2.024	2.022	2.027	1.987
Fo[a]	86.8	94.6	83.8	77.5	83.3	89.6	92.7	89.7	85.2	97.1	83.1	76.6	80.6	85.7

[a] Fo = Mg/(Mg + Fe) mol%.

Table 2
Average major and minor elements for pyroxene composition determined with EPMA.

	QUE 97008, 12			MET 00452, 16			NWA 8649			NWA 8276		
	c51	c61	c143	c150	c19	c111	c17 (core)	c17 (rims)	c87	c7	c69	c88
SiO2	54.18	54.43	51.78	52.60	55.58	56.09	55.04	56.35	54.91	52.64	55.96	55.63
TiO2	0.19	0.55	0.58	0.13	0.13	0.14	0.16	0.19	0.15	0.51	0.41	0.04
Al2O3	2.75	2.71	2.55	2.16	1.58	1.53	1.98	1.74	2.56	2.57	1.91	0.40
MgO	30.04	29.30	22.93	27.45	32.47	34.23	31.57	34.35	32.83	25.72	34.14	31.40
FeO	8.20	4.94	14.43	12.36	7.22	5.86	7.81	4.78	5.75	10.76	2.01	10.31
CaO	2.66	6.65	5.26	2.60	1.57	1.28	1.50	1.77	1.86	5.23	3.75	0.56
Na2O	0.01	0.01	0.00	0.01	0.00	0.00	0.00	0.00	−0.01	0.00	0.00	0.00
MnO	0.24	0.13	0.52	0.35	0.25	0.21	0.48	0.14	0.16	0.30	0.03	0.21
Cr2O3	1.52	1.08	1.09	1.18	1.31	1.00	1.19	0.84	1.48	1.24	1.04	0.78
Total	99.80	99.80	99.16	98.84	100.09	100.32	99.74	100.17	99.67	98.96	99.27	99.32
Si	1.926	1.921	1.921	1.924	1.950	1.946	1.944	1.947	1.927	1.923	1.941	1.980
Ti	0.005	0.015	0.017	0.004	0.003	0.004	0.004	0.005	0.004	0.014	0.011	0.001
Al	0.115	0.113	0.112	0.093	0.065	0.063	0.082	0.071	0.106	0.110	0.078	0.017
Sum	2.046	2.049	2.049	2.021	2.019	2.012	2.030	2.023	2.036	2.047	2.030	1.998
Mg	1.591	1.542	1.265	1.497	1.699	1.770	1.662	1.769	1.717	1.400	1.765	1.666
Fe	0.244	0.146	0.449	0.378	0.212	0.170	0.231	0.139	0.169	0.329	0.058	0.307
Ca	0.101	0.251	0.211	0.102	0.059	0.048	0.057	0.066	0.070	0.205	0.140	0.021
Mn	0.007	0.004	0.016	0.011	0.007	0.006	0.015	0.004	0.005	0.009	0.001	0.006
Cr	0.043	0.030	0.032	0.034	0.036	0.027	0.033	0.023	0.041	0.036	0.029	0.022
Na	0.001	0.001	0.000	0.001	0.000	0.000	0.000	0.000	−0.001	0.000	0.000	0.000
Sum Oct	1.987	1.973	1.973	2.022	2.013	2.021	1.997	2.001	2.001	1.979	1.993	2.023
Mg#[a]	86.7	91.4	73.5	79.8	88.9	91.2	87.8	92.7	91.1	81.0	96.8	84.5
En[b]	81.9	79.4	65.2	75.3	85.9	88.8	84.6	89.5	87.6	72.1	89.9	83.3
Wo[c]	5.2	12.9	10.9	5.1	3.0	2.4	2.9	3.3	3.6	10.5	7.1	1.1

[a] Mg# = Mg/(Mg + Fe) mol%.
[b] En = Mg/(Mg + Fe + Ca) mol%.
[c] Wo = Ca/(Mg + Fe + Ca) mol%.

Table 3
Average major and minor elements for plagioclase composition determined with EPMA.

	MET 00452, 16		NWA 8649		QUE 97008, 12				Semarkona	NWA 8276			
	c19	c111	c17	c87	c51	c61	c143	c150	c47	c7	c69	c87	c88
SiO2	45.46	46.90	44.73	44.87	45.86	46.13	46.55	45.72	44.88	45.59	45.32	44.84	44.28
TiO2	0.02	0.02	0.03	0.02	0.03	0.02	0.01	0.02	0.04	0.01	0.05	0.02	0.04
Al2O3	33.28	32.47	34.44	33.64	32.91	32.78	32.61	32.80	33.73	33.27	33.53	33.61	33.86
MgO	0.83	0.87	0.64	0.75	0.74	0.98	0.78	0.74	0.72	0.80	0.85	0.73	0.61
FeO	0.63	0.85	0.32	0.52	0.85	0.43	1.04	0.96	0.90	0.81	0.31	1.34	0.90
CaO	19.39	19.01	19.13	18.75	18.94	19.32	18.70	18.91	19.25	19.27	19.35	19.21	19.34
Na2O	0.23	0.24	0.73	0.77	0.42	0.17	0.40	0.36	0.05	0.15	0.14	0.29	0.05
K2O	0.00	0.00	0.00	0.00	0.00	−0.01	0.00	0.00	0.00	0.00	0.01	0.03	0.03
MnO	0.00	−0.01	0.01	0.00	0.01	0.01	0.00	−0.01	0.02	0.01	0.00	0.02	0.02
Total	99.84	100.37	100.04	99.33	99.76	99.84	100.12	99.51	99.60	99.93	99.55	100.08	99.13
Si	2.108	2.158	2.071	2.091	2.127	2.134	2.150	2.127	2.088	2.112	2.103	2.083	2.072
Al	1.818	1.761	1.879	1.848	1.799	1.787	1.775	1.799	1.849	1.816	1.834	1.840	1.868
Ca	0.963	0.938	0.949	0.936	0.941	0.958	0.925	0.942	0.959	0.957	0.962	0.956	0.970
Na	0.021	0.021	0.065	0.070	0.037	0.015	0.036	0.033	0.004	0.014	0.012	0.026	0.005
K	0.000	0.000	0.000	0.000	0.000	0.000	0.000	0.000	0.000	0.000	0.000	0.002	0.002
Mg	0.058	0.060	0.044	0.052	0.051	0.068	0.054	0.051	0.050	0.056	0.059	0.051	0.042
Fe	0.025	0.033	0.013	0.020	0.033	0.017	0.040	0.037	0.035	0.031	0.012	0.052	0.035
Mn	0.000	0.000	0.000	0.000	0.000	0.000	0.000	0.000	0.001	0.000	0.000	0.001	0.001
End-Member proportions													
$Ca(Fe,Mg,Mn)Si_3O_8$	0.069	0.080	0.033	0.046	0.071	0.078	0.071	0.070	0.059	0.070	0.060	0.068	0.056
$KAlSi_3O_8$	0.000	0.000	0.000	0.000	0.000	0.000	0.000	0.000	0.000	0.000	0.001	0.001	0.002
$NaAlSi_3O_8$	0.016	0.021	0.049	0.056	0.036	0.014	0.032	0.029	0.002	0.013	0.011	0.018	0.004
$CaAl_2Si_2O_8$	0.891	0.857	0.906	0.883	0.870	0.879	0.852	0.870	0.899	0.885	0.901	0.884	0.912
$(Fe,Mg,Mn)Al_2Si_2O_8$	0.010	0.012	0.008	0.012	0.012	0.008	0.019	0.015	0.024	0.016	0.010	0.026	0.019
$[]Si_4O_8$	0.013	0.028	0.000	0.000	0.011	0.021	0.024	0.015	0.015	0.015	0.017	0.001	0.007
An[a]	97.9	97.8	93.6	93.1	96.2	98.5	96.3	96.7	99.6	98.6	98.7	97.2	99.4

[a] An = Ca/(Ca + Na + K) mol%.

phenocrysts. The plagioclase grains, which are interstitial to the pyroxene grains and the olivine phenocrysts, have a composition of $\sim An_{98}$.

NWA 8276 c87 (Fig. 2d) is a large (~800 μm) type II-POP chondrule, in which olivine phenocrysts are small and homogeneously distributed. The olivine core compositions are $\sim Fo_{83}$ with zoning toward the rims. The pyroxene grains are very small and occur along the rims of the olivine phenocrysts. The plagioclase occurs as euhedral, elongated grains with a composition of $\sim An_{97}$.

QUE 97008 c150 (Fig. 2e) is mainly composed of large olivine phenocrysts with small low-Ca pyroxene in between and interstitial plagioclase grains. The olivine phenocrysts are homogeneous ($\sim Fo_{77}$). The low-Ca pyroxene grains are interstitial between the olivine phenocrysts with a composition of $Wo_3En_{89}Fs_8$. The plagioclase grains have a composition of $\sim An_{97}$. One olivine phenocrysts on the edge of the chondrule (upper left corner in Fig. 2e) shows complex zoning with a core of $\sim Fo_{95}$, then a diffuse zonation toward $\sim Fo_{97}$, surrounded by olivine that approaches the composition of the other olivine grains ($\sim Fo_{80}$) in this chondrule.

Semarkona c47 (Fig. 2f) is a large chondrule (~1.5 mm) mainly composed of small olivine phenocrysts. The olivine phenocrysts are homogeneous ($\sim Fo_{86}$) and have small overgrowths of high-Ca pyroxene that were too small to be accurately analyzed (i.e., below a few μm). The plagioclase grains are interstitial to the pyroxene grains and the olivine phenocrysts and have nearly endmember anorthite composition ($\sim An_{100}$).

NWA 8276 c88 is clearly mineralogically zoned, with only anorthite grains, small high-Ca pyroxene grains and euhedral FeO-rich olivine phenocrysts in its core (Fig. 2g). The low-Ca pyroxene grains are only located in the rim of the chondrule, with abundant rounded inclusions of olivine (i.e., named chadacrysts in Jones, 1989) and have composition of $Wo_1En_{83}Fs_{16}$. The Fo contents of the olivine chadacrysts in the low-Ca pyroxene grains are higher ($\sim Fo_{80}$) than the Fo contents of the euhedral olivine phenocrysts in the core of the chondrule ($\sim Fo_{77}$). Additionally, some zoning can be observed in the low-Ca pyroxenes at the boundary between the core and rim of the chondrule, with slightly lower Mg# (~75 mole%) and higher Ca content in the core than in the rim (Mg# ~84 mole%). Plagioclase compositions are nearly pure anorthite with An_{99}.

Semarkona c34 (formally named as CH23 in Kita et al., 2000, 2010; Tachibana et al., 2003) is also mineralogically zoned with large olivine phenocrysts in the center of the chondrule, while low-Ca pyroxene grains are only located in the

rim of the chondrule, with rounded inclusions of olivine grains (Fig. 2h). Kita et al. (2000) determined the olivine chadacrysts to have Mg# of 82 mole% and the low-Ca pyroxene to have a composition of $Wo_{2-5}En_{76-82}Fs_{16-19}$. The plagioclase compositions are nearly pure anorthite with An_{100}.

A good example of the distribution of O and Al-Mg isotopes analyses is illustrated for the Semarkona c34 chondrule in Fig. 3.

3.1.3. Mineral chemistry

The Mg# of olivine and pyroxene range from 77 to 97. In most chondrules, both olivine and pyroxenes are homogeneous in Mg#, with internal variations less than 1% (1SD). Fo content of olivine and En content of low-Ca pyroxene are usually in agreement within ±2 mole%, even for NWA 8649 c17 where only pyroxene analyses were taken from the rims. Olivine grains of all chondrules have Mn compositions that lie between type II-PO chondrule olivine grains from ordinary chondrites (OC line, Fig. 4a) and CO chondrites (CO line, Fig. 4a) (Berlin et al., 2011). The Cr_2O_3 contents of ferroan olivine core for all chondrules are between 0.2–0.8 wt% and exhibit a slight decrease with increasing FeO contents (Fig. 4b), typical for olivine grains of chondrules from UOCs of low subtypes 3.00–3.05 (Grossman and Brearley, 2005).

Some chondrules have euhedral plagioclases, usually euhedral elongated grains (NWA 8276 c7, c87, c88; MET 00452 c19; Semarkona c34; QUE 97008 c51, c143, c150), whereas others have more interstitial shaped grains with habitus delineated by the surrounding mineral grains (NWA 8276 c69; MET 00452 c111; Semarkona c47; QUE 97008 c61; NWA 8649 c17 and c87). No zonation is observed at the rim of anorthite grains for all studied chondrules. The plagioclases selected for this study are mostly pure anorthite (An > 95%), with only two chondrules from NWA 8649 (c17 and c87) that have plagioclase compositions of $\sim An_{93}$ and $\sim An_{94}$, respectively. The measured plagioclase compositions in this study is only 85–91 mole% $CaAl_2Si_2O_8$ due to both the incorporation of Fe and Mg and because the $NaAlSi_3O_8$ endmember only account for 0.2–6.0 mole%. They have extremely low $KAlSi_3O_8$ concentrations, usually well below 1%. Silica excess is found in all chondrules except both chondrules from NWA 8649. There is a correlation between An content and silica excess (Fig. 5a) although the small range of An composition for these plagioclases grains precludes any robust interpretation. Their MgO contents are mostly between 0.5 and 1 wt%, with only 3 analyses higher than 1 wt% (Fig. 5b). The Mg and Fe contents of plagioclases are clearly related to the substitution (5) for all chondrules with Ca(Mg,Fe,Mn)Si_3O_8 end-members between 3 and 8 mole%. (Mg,Fe,Mn)$Al_2Si_2O_8$ end-member only account for a minor amount of Mg and Fe incorporation with end-members between 0.8 and 2.6 mole%.

3.2. Oxygen three-isotopes

Table 4 shows the mean values for $\delta^{18}O$, $\delta^{17}O$ and $\Delta^{17}O$ for all chondrules studied in this paper. Among the 14 chondrules, NWA 8276 c69 exhibits large variations in both $\delta^{18}O$ and $\delta^{17}O$ after the instrumental bias correction, which are likely related to a large hole in the sample surface near the chondrule. The SIMS secondary ion deflector (DTFA-XY) adjustments exceeded their normal range (±50 bits) for this chondrule, which is known to create larger analytical fractionation for O isotopes (Kita et al., 2009). Therefore, we decided not to include $\delta^{18}O$ and $\delta^{17}O$ values of this chondrule in the final reported values. Nevertheless, instrumental fractionations on $\delta^{18}O$ and $\delta^{17}O$ are mass-dependent, so that the $\Delta^{17}O$ values are not affected and reported in the Table 4. Except for NWA 8276 c69, individual SIMS spot analyses of each chondrule are shown in Figs. 6 and 7.

Half of the chondrules studied here show a small variation in $\delta^{18}O$ and $\delta^{17}O$ beyond their analytical uncertainties. Seven chondrules have internally homogeneous olivine and pyroxene isotope ratios throughout the entire chondrule, i.e., QUE 97008 c51 (Fig. 6a), NWA 8276 c87 (Fig. 6b), Semarkona c47 (Fig. 6c), c34 (Fig. 6d), MET 00452 c19 (Fig. 6e), c111 (Fig. 6f) and NWA 8649 c17 (Fig. 7g). In contrast, some O isotope data for individual chondrules shows a clear spread along a 1:1 line, such as NWA 8276 c7 (Fig. 7a) and NWA 8276 c88 (Fig. 7b), while others show mass dependent fractionation (slope = 0.52), such as QUE 97008 c61 (Fig. 7c), c143 (Fig. 7d), c150 (Fig. 7e), NWA 8649 c87 (Fig. 7f). The data excluded from the computation of the host chondrule values are displayed as slightly transparent in Figs. 6 and 7. One chondrule contained what seems to be a relict olivine at its edge (QUE 97008 c150, Fig. 2d), that exhibits Fe-Mg zoning and has significantly different O isotope ratios compared to the rest of analyses in this chondrule. Interestingly, the analyses of the core of the relict olivine grain gave only slightly lower values ($\delta^{18}O = 3.86 \pm 0.26‰$, $\delta^{17}O = 1.85 \pm 0.20‰$) than the rest of the analyses ($\delta^{18}O = 4.54 \pm 0.40‰$, $\delta^{17}O = 2.34 \pm 0.42‰$), see EA1. On the other hand, an analysis from the rim of this grain gave very different results than the rest of the olivine analyses ($\delta^{18}O = 5.44 \pm 0.26‰$, $\delta^{17}O = 3.86 \pm 0.20$). Both analyses were removed from the computation of the mean for this chondrule.

The host chondrule $\delta^{18}O$ values range from 3.45 ± 0.36‰ (2SE) to 5.64 ± 0.47‰ (2SE). The $\delta^{17}O$ values range from 1.36 ± 0.32‰ to 3.29 ± 0.29‰. The $\Delta^{17}O$ values range from −0.44 ± 0.23‰ to 0.49 ± 0.15‰ with the mean value of 0.05 ± 0.51‰ (2SD, $n = 14$). The host chondrule data fall on a steeper slope than the terrestrial mass fractional line (slope = 0.52), with an approximate slope of 1 (Fig. 8a). They all fall between the Equilibrated Chondrite Line (ECL, Clayton et al., 1991) and the Primitive Chondrule Minerals line (PCM, Ushikubo et al., 2012). Overall, the chondrules have O three isotope compositions that are in good agreement with the plagioclase-bearing chondrules of UOCs from Kita et al. (2010) and tend to show at the lowest end of $\Delta^{17}O$ distributions among LL3 chondrules (mean value of 0.5 ± 0.9‰, 2SD, $n = 33$). Chondrules within a single chondrite form clusters of data (Fig. 8a), except for NWA 8276 in which c87 is at the lower end of the cloud of values whereas the two other chondrules are at the higher end. No correlation between Mg# and O three isotopes was found (Fig. 8b).

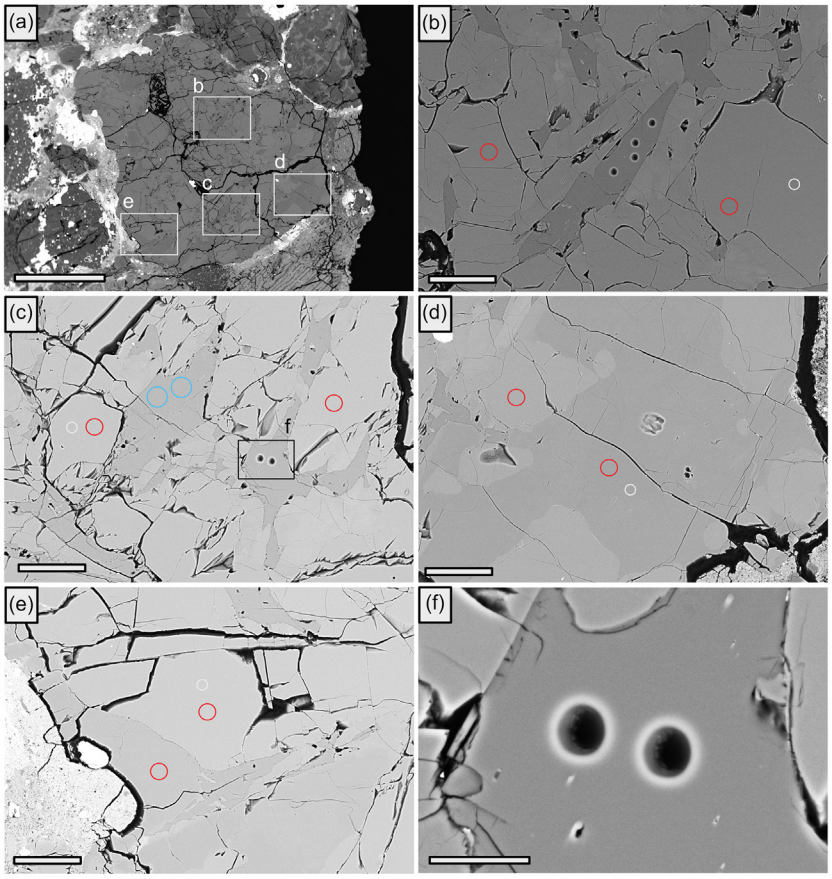

Fig. 3. Example of chondrule petrography (Semarkona c34), with locations of the different type of analyses made. Red spots refer to the locations of oxygen isotope analyses, white spots are for olivine-pyroxene Al-Mg isotope analyses, blue spots correspond to locations of anorthite MCFC analyses and visible spots are actual spots of FC-EM analyses of anorthite grains. (For interpretation of the references to colour in this figure legend, the reader is referred to the web version of this article.)

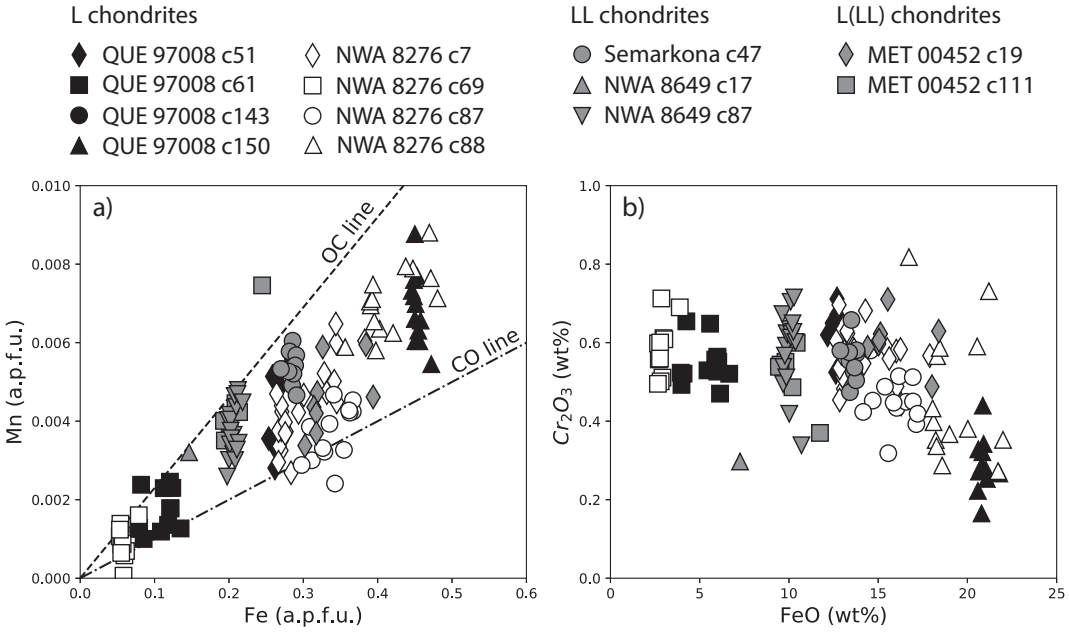

Fig. 4. Composition of olivine analyses from the studied chondrules. (a) Fe (a.p.f.u.) vs Mn (a.p.f.u.) diagram with OC (chondrule olivines from ordinary chondrites) and CO (chondrule olivines from CO chondrites) lines from Berlin et al. (2011). (b) FeO (wt%) vs Cr_2O_3 (wt%) diagram. a.p.f.u = atoms per formula unit.

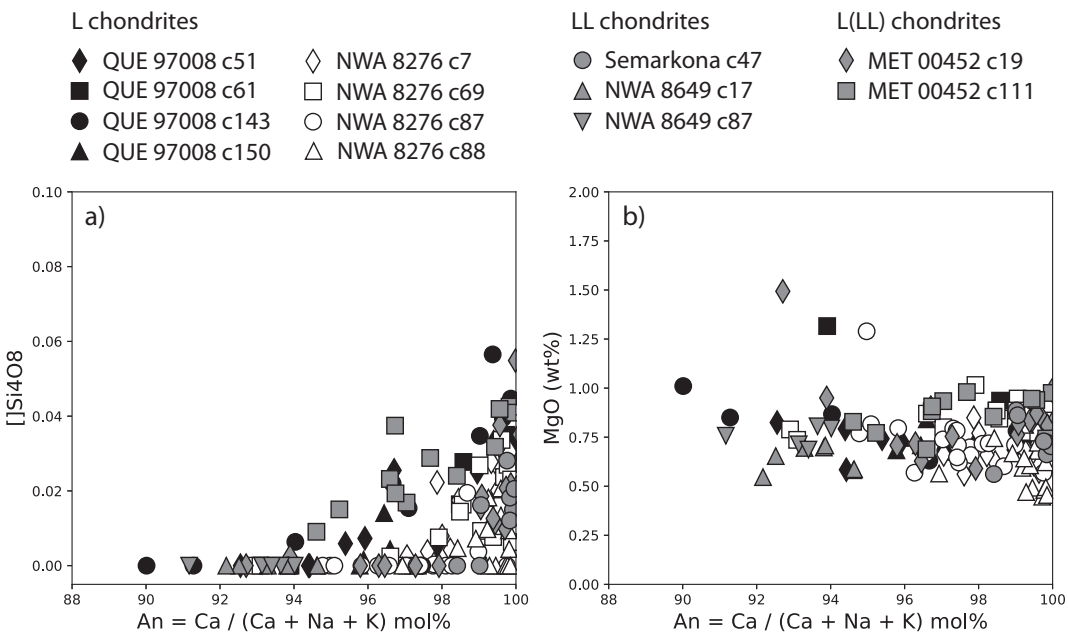

Fig. 5. Composition of plagioclase grains analyzed from the selected chondrules. (a) Anorthite content (calculated as Ca/(Ca + Na + K) mol %) vs excess silica ($[]Si_4O_8$); (b) Anorthite content vs MgO (wt%) content.

Additionally, two analyses of plagioclase were obtained in two chondrules NWA 8276 c7 and c88, where the plagioclase grains were big enough to measure with 12 µm spots. The plagioclase analyses in NWA 8276 c7 (Fig. 7a) are slightly deviated to higher $\delta^{17}O$ and $\delta^{18}O$ compared to those of the olivine and pyroxene analyses, though data from plagioclase in c88 overlaps with the olivine and pyroxene analyses in the same chondrule (Fig. 7b). In both cases, the differences between the plagioclase and the host chondrules are less than 1‰, which is much smaller than is the case for glassy mesostasis in LL3.0–3.1 chondrules (as high as ~10‰; Kita et al., 2010).

3.3. Al-Mg systematics

Between 8 and 18 analyses were done in each chondrule (Table 5). In each chondrule, four analyses of pyroxene and/or olivine grains were measured. In Semarkona c34,

Table 4
Host oxygen three isotope ratios of anorthite bearing chondrules.

Chondrule	*n*	Type	$\delta^{18}O$	Unc.	$\delta^{17}O$	Unc.	$\Delta^{17}O$	Unc.	Mg#[a]
QUE 97008									
c51	7	II-PO	3.89	0.34	2.21	0.25	0.18	0.16	87
c61	7	I-POP	3.96	0.47	2.21	0.27	0.15	0.12	95
c143	8	II-PO	4.83	0.36	2.75	0.21	0.24	0.09	84
c150	8	II-POP	4.54	0.40	2.34	0.35	−0.02	0.32	87
MET 00452									
c19	7	II-PO	4.30	0.35	2.14	0.28	−0.10	0.23	83
c111	8	II-POP	4.04	0.33	2.27	0.20	0.17	0.14	90
Semarkona									
c34	8	II-POP	4.48	0.33	2.45	0.24	0.12	0.19	82
c47	8	II-PO	4.45	0.35	2.26	0.29	−0.05	0.23	86
NWA 8649									
c17	8	I-PP	3.45	0.36	1.36	0.32	−0.44	0.23	93
c87	6	II-PO	3.62	0.40	1.72	0.25	−0.16	0.10	90
NWA 8276									
c7	6	II-PO	5.64	0.47	3.29	0.29	0.36	0.17	85
c69	6	I-POP					0.49	0.15	97
c87	8	II-PO	3.59	0.33	1.54	0.22	−0.33	0.13	83
c88	8	II-POP	5.13	0.51	2.81	0.34	0.15	0.20	80

[a] Mg# = Mg/(Mg + Fe) mole%.

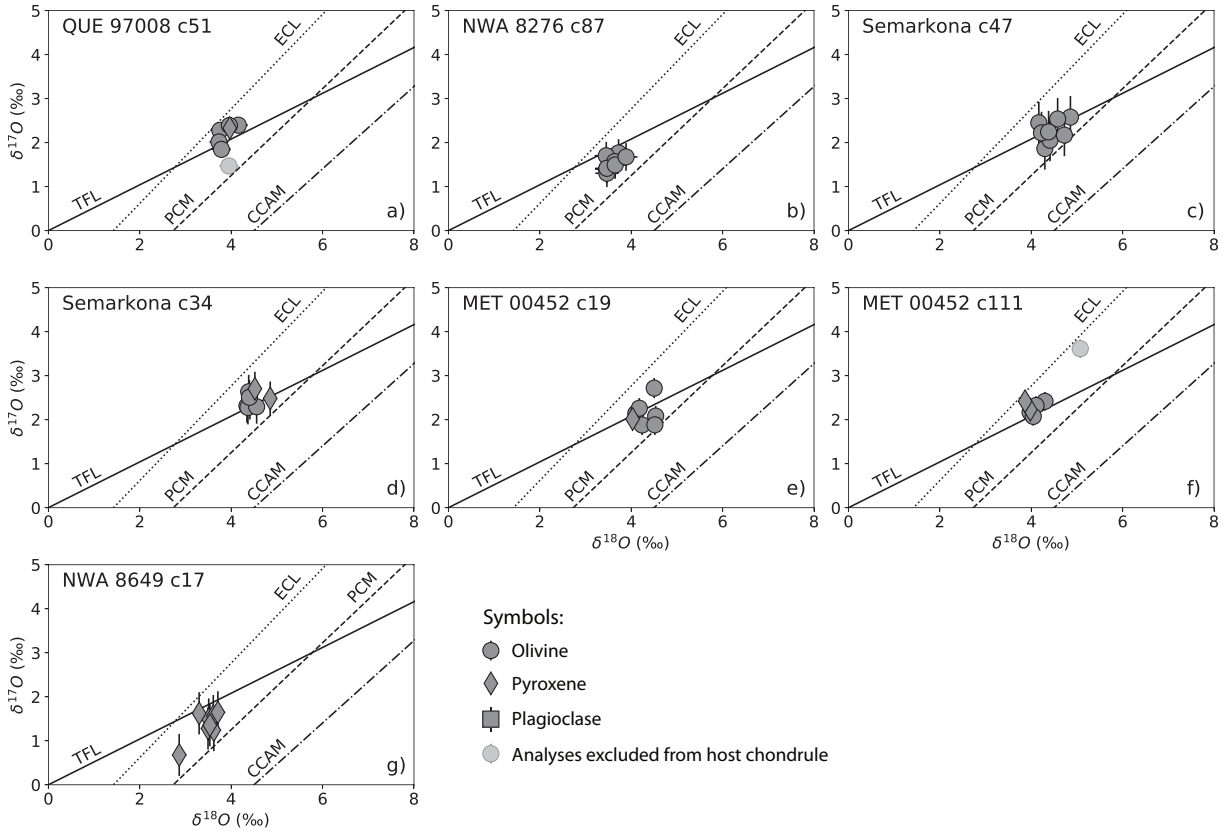

Fig. 6. Individual oxygen three-isotope analyses of of 7 studied chondrules. (a) QUE 97008 c51, (b) NWA 8276 c87, (c) Semarkona c47, (d) Semarkona c34, (e) MET 00452 c19, (f) MET 00452 c11, (g) NWA 8649 c17. Symbols of minerals are as follows, dots: olivine, diamonds: pyroxene and squares: plagioclase. Error bars represent 2SD of bracketing standards. Transparent symbols represent data not used for the computation of the host chondrule values.

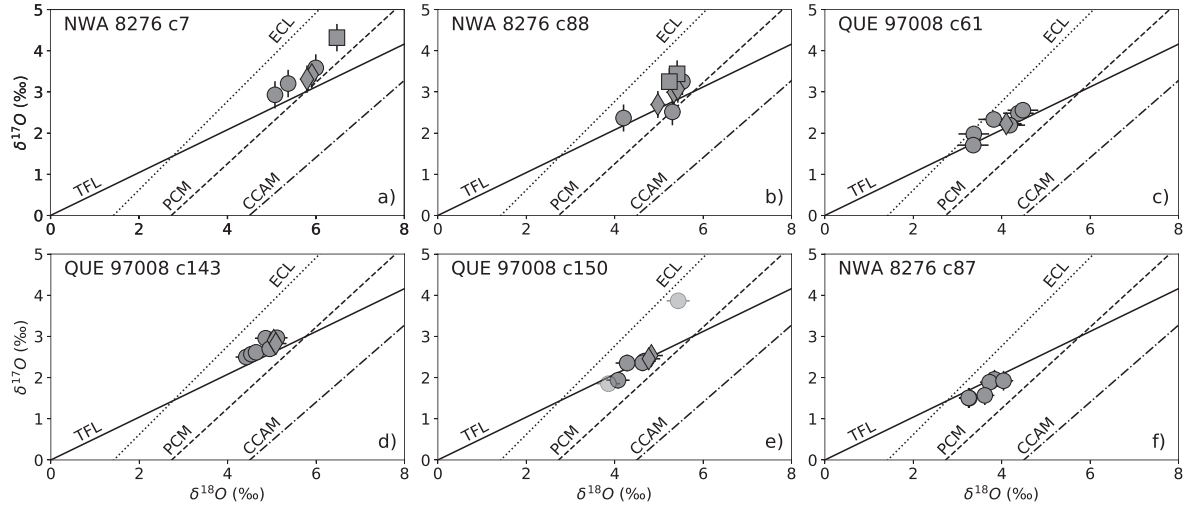

Fig. 7. Individual oxygen three-isotope analyses of remaining 6 chondrules studied. (a) NWA 8276 c7, (b) NWA 8276 c88, (c) QUE 97008 c61, (d) QUE 97008 c143, (e) QUE 97008 c150, (f) NWA 8276 c87. Symbols of minerals are the same as in those Fig. 6. Error bars represent 2SD of bracketing standards. Transparent symbols represent data not used for the computation of the host chondrule values.

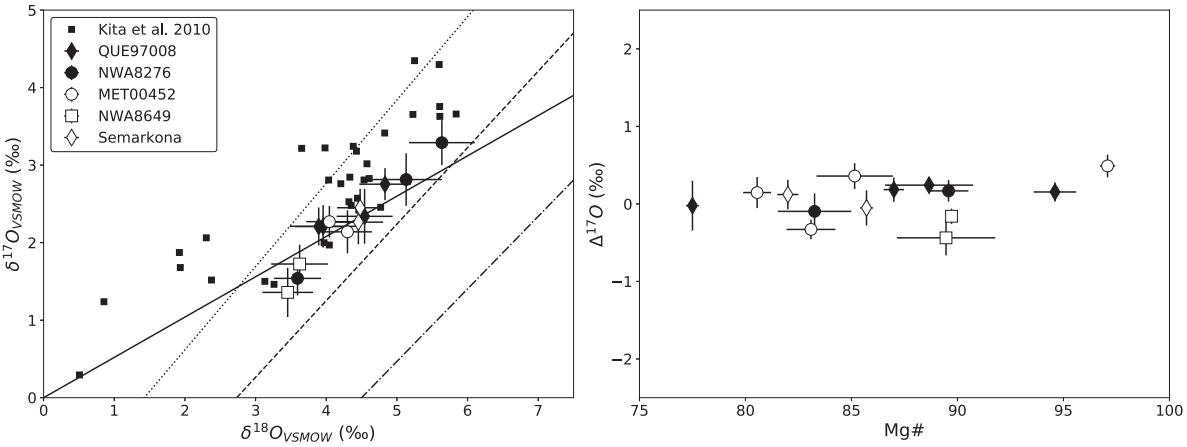

Fig. 8. (a) Host chondrule $\delta^{18}O$ vs $\delta^{17}O$ plot of 13 chondrules, except for NWA 8276 c69 (see text for explanation). Error bars represent 2SE. (b) Host chondrule $\Delta^{17}O$ values vs Mg# of olivine/pyroxene. Error bars represent 2SE.

four MCFC analyses were possible in anorthite grains, in NWA 8276 c69 only three MCFC points were measured and, finally, in NWA 8276 c88, five MCFC points were determined. Since all plagioclase grains analyzed during this study are very close to pure anorthite in composition and has between 0.5 and 1 wt.% MgO, the $^{27}Al/^{24}Mg$ ratios are all between 33 and 76. Usually, the Al-Mg isochrons are drawn through two clusters of points, pyroxenes/olivines near the origin and plagioclases for high Al/Mg ratios. In this case, most of the chondrules exhibit some variations for the plagioclases measured, with the $^{27}Al/^{24}Mg$ ratios typically vary by 10–15. Some chondrules show even larger spreads in Al/Mg ratios in plagioclases such as NWA 8276 c88 from 45 to 76 or MET 00452 c111 from 41 to 66. On the other hand, some chondrules have plagioclase $^{27}Al/^{24}Mg$ ratios that show small variabilities $\leq$10, such as QUE 97008 c61 and c150, NWA 8649 c17, NWA 8649 c87, Semarkona c47, or NWA 8276 c69. All analyses of plagioclases exhibit resolvable excesses in ^{26}Mg, which range between 1.0 ± 0.4‰ and 4.8 ± 0.6‰. The $^{27}Al/^{24}Mg$ ratios of pyroxene grains are generally higher (from 0.003 to 0.08) than olivine grains (1×10^{-4}–7×10^{-3}). The $\delta^{26}Mg^*$ values of the olivines and pyroxenes are all within uncertainty of the measurements, ±0.10‰. The Al-Mg isochron regressions of individual chondrules are well-behaved, with MSWD between 0.37 and 1.8, except for one chondrule NWA 8649 c87 that will be discussed later. These values are very significant since the degrees of freedom range between 6 and 14, and higher degrees of freedom require MSWD that are closer to 1 to be considered as isochrons (Wendt and Carl, 1991). The $(^{26}Al/^{27}Al)_0$ of the chondrules range from $(6.3 \pm 0.4) \times 10^{-6}$ to $(8.9 \pm 0.2) \times 10^{-6}$ (Table 5). The inferred $(^{26}Al/^{27}Al)_0$ of chondrules are converted into relative crystallization ages after CAIs using the canonical value of 5.25×10^{-5} (Jacobsen et al., 2008; Larsen et al., 2011) under the assumption of a homogeneous distribution of ^{26}Al in the early Solar System (Kita et al., 2013; Budde et al., 2018). The range of ages from these chondrules is between 1.80 ± 0.04 Ma to 2.16 $\pm$ 0.11 Ma after CAIs. The intercepts of all regressions $(\delta^{26}Mg^*)_0$ range between -0.043 ± 0.046‰ (2SD) and $+0.046 \pm 0.046$‰ (2SD). They all are indistinguishable from 0 within errors. Ages obtained for the two chondrules using both MCFC and FC-EM methods are similar within errors (Semarkona c34 and NWA 8276 c88, see Table 5). The errors for age represent 95% confidence interval, they range from 0.04 Ma to 0.16 Ma.

Of the 14 chondrules analyzed, only one chondrule NWA 8649 c87 resulted in an errorchron with a MSWD of 4.7 when taking all analyses. However, only one point was significantly lower than the rest (Pl #2 in EA3). When comparing the SE and BSE images of SIMS spots for all anorthite analyses, no clear evidence was found to reject this analysis. We choose to remove this point from the fit and it results in a MSWD of 2.1, within acceptable bound for this degree of freedom. Isochron diagrams of QUE 97008 c143 and c150, MET 00452 c111, and NWA 8276 c69 also show small scatter from regression lines, which are not as significant as NWA 8649 c87. Their MSWD are from 1.2 to 1.8, which are acceptable ranges.

It is evident that chondrules in QUE 97008 have a younger age than the chondrules from the other chondrites, except NWA 8276 c69. Some chondrules from the same meteorite yield ages that are resolved from each other. For example, NWA 8276 c69 (2.04 ± 0.07 Ma) is younger than the other chondrules in the same meteorite (mean age of 1.86 ± 0.10 Ma). Similarly, chondrules in QUE 97008 seems to have two population of ages, with chondrules c51 and c61 at 2.00 ± 0.04 Ma and 2.00 ± 0.06 Ma, respectively, compared to chondrules c143 and c150 that have ages of 2.16 ± 0.06 Ma and 2.13 ± 0.07 Ma, respectively. We also note that some of these chondrules are those with slightly scattered data on the isochron diagrams. Interestingly, both QUE 97008 and NWA 8276 are L chondrites. Indeed, all ages younger than 1.95 Ma are found in these two chondrites. L(LL) and LL chondrites only have chondrules with ages comprised between 1.80 ± 0.04 Ma and 1.94 ± 0.08 Ma. Since the differences in the $\Delta^{17}O$ values of these chondrules types are smaller than the uncertainty of the SIMS analyses (e.g., Fig. 8b), no correlation between Al-Mg ages and $\Delta^{17}O$ values is found.

Table 5
Summary of Al-Mg chronology of anorthite-bearing chondrules.

Chondrule	*n*	Type	MSWD	slope	unc.	$\delta^{26}Mg_0$ (‰)	unc.	$(^{26}Al/^{27}Al)_0 \times 10^{-6}$	unc. $\times 10^{-6}$	Δt_{CAIs} (Ma)	unc.
QUE 97008											
c51	10	II-PO	1.1	0.0526	0.0046	−0.004	0.044	7.33	0.64	2.00	0.09
c61	9	I-POP	0.67	0.0526	0.0058	0.041	0.042	7.33	0.81	2.00	0.11
c143	10	II-PO	1.6	0.0449	0.0050	−0.001	0.046	6.26	0.70	2.16	0.11
c150	8	II-POP	1.2	0.0464	0.0066	−0.005	0.046	6.46	0.92	2.13	0.15
MET 00452											
c19	16	II-PO	1.2	0.0574	0.0036	0.046	0.046	8.00	0.50	1.91	0.06
c111	16	II-POP	1.8	0.0609	0.0036	−0.004	0.048	8.48	0.50	1.85	0.06
Semarkona											
c47	9	II-POP	0.7	0.0558	0.0044	−0.017	0.044	7.77	0.61	1.94	0.08
c34 (FC-EM)	12	II-PO	0.37	0.0598	0.0040	−0.042	0.046	8.33	0.56	1.87	0.07
c34 (FC-FC)	8		0.66	0.0594	0.0034	−0.043	0.046	8.28	0.47	1.88	0.06
c34 (all)	16		0.45	0.0595	0.0026	−0.043	0.046	8.29	0.36	1.88	0.04
NWA 8649											
c17	12	I-PP	1.3	0.0621	0.0038	−0.004	0.054	8.65	0.50	1.83	0.06
c87	11	II-PO	2.1	0.0572	0.0046	−0.030	0.044	7.97	0.64	1.92	0.08
NWA 8276											
c7	15	II-PO	1.2	0.0586	0.0032	−0.003	0.042	8.16	0.45	1.89	0.06
c69	10	I-POP	1.8	0.0509	0.0036	0.036	0.044	7.09	0.50	2.04	0.07
c87	10	II-PO	1.8	0.0596	0.0038	0.000	0.044	8.30	0.53	1.88	0.06
c88 (FC-EM)	13	II-POP	1.2	0.0624	0.0032	−0.035	0.048	8.69	0.45	1.83	0.05
c88 (FC-FC)	9		0.51	0.0650	0.0026	−0.033	0.048	9.06	0.36	1.79	0.04
c88 (all)	18		1.1	0.0639	0.0022	−0.031	0.048	8.90	0.31	1.80	0.04

4. DISCUSSION

4.1. Igneous fragment vs chondrule origin

The first description of anorthite-bearing UOC chondrules was in Hutcheon and Hutchison (1989), which they called "clast chondrule". They obtained a well-defined Al-Mg isochron with an initial $^{26}Al/^{27}Al$ ratio of $(7.7 \pm 2.1) \times 10^{-6}$, which translated to the age of 1.95 ± 0.29 Ma after CAIs. The object they studied had an irregular shape and minerals at its edge were terminated abruptly against the chondrule border. Additionally, the bulk composition showed the absence of volatiles with a very low Na/Al ratio and the REE patterns in the pyroxene and plagioclase were fractionated. Based on these observations, they concluded that it represents a fragment of an igneous rock. Even if the chondrules studied in this paper resembled the object described by Hutcheon and Hutchinson (1989), several aspects challenge their interpretation. First, most of the chondrules presented here are rounded and do not seemed to represent fragments of either chondrules or igneous clasts. Second, the Mg# of both olivine and pyroxene grains span a wide range of compositions (from 76.6 ± 0.7 to 97.1 ± 0.4), which makes it hard to explain them as the products of igneous crystallization in a single asteroidal body. At least one chondrule exhibits clear mineralogical zoning (NWA 8276 c88, Fig. 2g), with low-Ca pyroxene in the rim with rounded inclusion of olivine ($Fo_{80.6 \pm 0.7}$) and euhedral grains of olivine ($Fo_{76.6 \pm 0.7}$) and anorthite in the core. Additionally, pyroxenes exhibit a diffuse zoning at the boundary between rim and core (see EA6 c88 image A), with higher FeO contents in the core. The mineral zoning from rim to core and the texture of the core indicate that a sequence of crystallization started from the outer rim to the inner core. Thus, they represent chondrules that were heated at high temperatures and cooled from their peripheries, rather than fragments of igneous objects. Additionally, the $\Delta^{17}O$ values are slightly variable among anorthite bearing chondrules, which argue against their origin from a single igneous object. The O isotopes signatures for these chondrules overlaps significantly to other chondrules from UOCs (Kita et al., 2010), suggesting a common formation regions for these anorthite-bearing chondrules and typical UOCs chondrules.

Even though the studied chondrules do not represent the most common type of chondrules in ordinary chondrites, they have been widely used for Al-Mg chronology (Kita et al., 2000; Mostefaoui et al., 2002; Tachibana et al., 2003). Several large chondrules studied for both Pb-Pb and Al-Mg age determinations by Bollard et al. (2019) seem to contain anorthite-rich plagioclase. Tachibana et al. (2003) obtained a bulk chondrule composition for one of the chondrules studied here (Semarkona c34) and compared its major element composition to other, more typical, type-II chondrules. It seems to have more refractory elements (Ca and Al) and less volatiles elements (Na and Mn) than other type-II chondrules from Semarkona. This is in agreement with the observation of lower Mn content in olivine (Fig. 4a) and the very high An content of plagioclases. Since Mn condenses more at higher temperature than Na in dust-enrich system (e.g., 100 × Solar composition gas; Ebel and Grossman, 2000), the very low Na/Ca ratios of these chon-

drules could be explained by heating at temperatures lower than condensation of Mn, where Na would have been evaporated. Alternatively, these chondrules could have formed form Na and Mn depleted precursors that were enriched in refractory elements. Either cases, these chondrules are different from typical UOC chondrules, in which the partitioning of Na between olivine and glass shows little evidence for Na evaporation indicative of a high dust density ($10^6 \times$ Solar composition gas) in the local disk environments that could have prevent evaporation of Na (Alexander et al., 2008).

4.2. Minimal secondary effects on Al-Mg system

Several observations points toward the fact that the extent of parent-body metamorphism has not significantly modified the Al-Mg system of the studied chondrules. First, we have selected a suite of least metamorphosed UOCs (3.00–3.05) based on the Cr_2O_3 contents in olivine (Grossman and Brearley, 2005), as also shown from olivine analyses of individual chondrules with consistently high Cr_2O_3 contents (Fig. 4b). Second, the presence of excess silica in plagioclases in almost all chondrules, except the two chondrules from NWA 8649, are at similar levels to the primitive Acfer 094 (ungrouped C3.00) and CR chondrites, which experienced minimal thermal metamorphism (Tenner et al., 2019). Third, the well-behaved ^{26}Al-^{26}Mg isochron (MSWD ~1) for most chondrules (Figs. 9 and 10). Particularly, excess silica has been shown to occur only in very high temperature plagioclase, i.e., 1100–1500 °C (Longhi and Hays, 1979). Any subsequent parent body metamorphism and/or aqueous alterations would have resulted in the elimination of the excess silica content, incorporation of alkali elements, as well as formation of secondary phases such as nepheline, sodalite, and clay minerals, which are not observed from chondrules in this study. Van Orman et al. (2014) discussed the time required for modifying Al-Mg ages in plagioclase as a function of grain sizes and self-diffusion coefficient at given temperatures and plagioclase compositions. According to the results given by Van Orman et al. (2014), the ^{26}Al-^{26}Mg age would be reset by 0.7 Ma (one half-life, i.e., 50% loss of excess ^{26}Mg) in a 20 μm spherical anorthite grain (10 μm radius) by 0.56 Ma at 500 °C and 1363 Ga at 300 °C. Since Semarkona is known to have never experienced parent body temperatures higher than 260 °C (Alexander et al., 1989), resetting the two Semarkona chondrules studied here is impossible. All chondrites selected for this work are low subtype UOCs

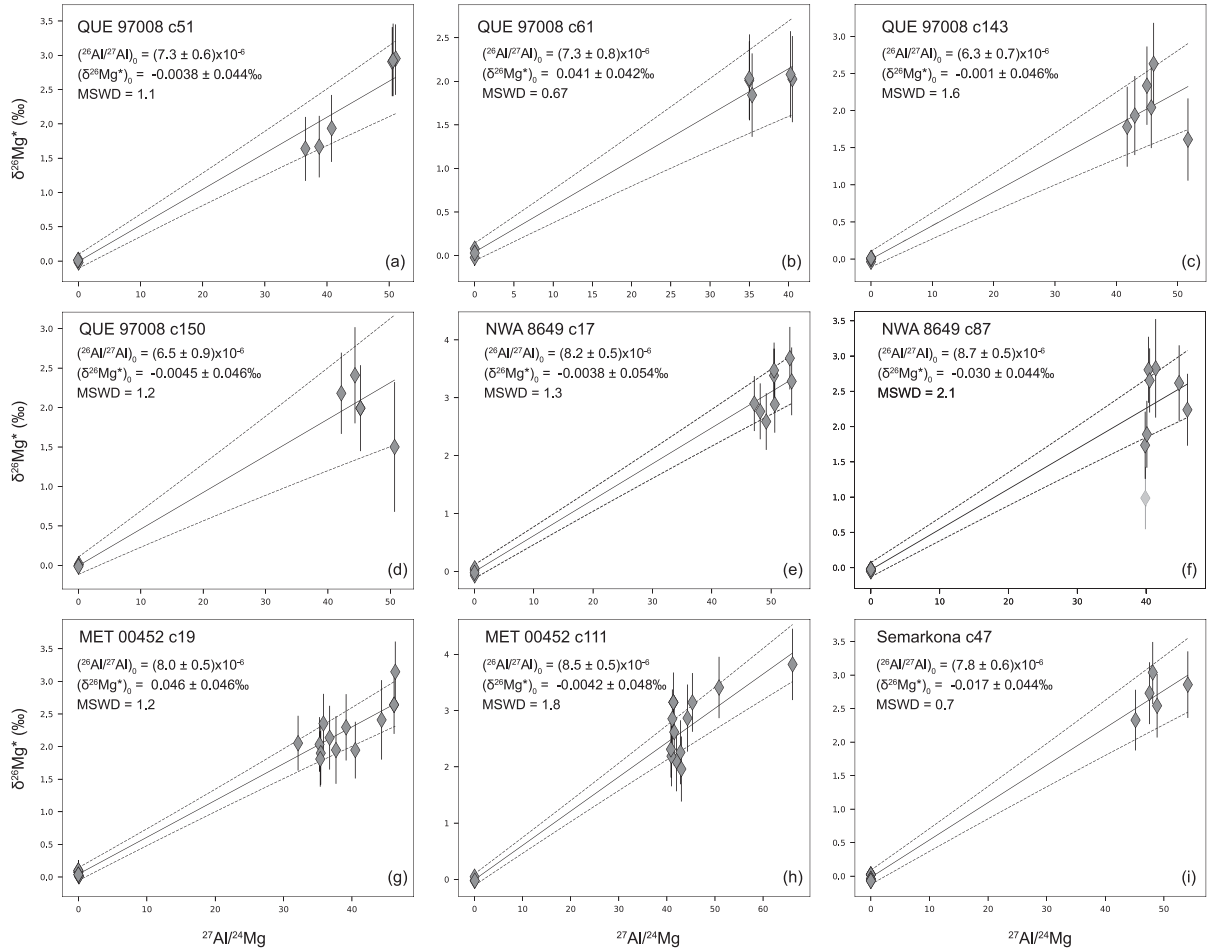

Fig. 9. Internal isochron regression for 9 studied chondrules in this study. Error bars represent 2SE. The solid lines represent the regressions and dash lines are 95% confidence interval on the fit. Uncertainties for $(^{26}Al/^{27}Al)_0$ and $(\delta^{26}Mg^*)_0$ are 95% confidence level.

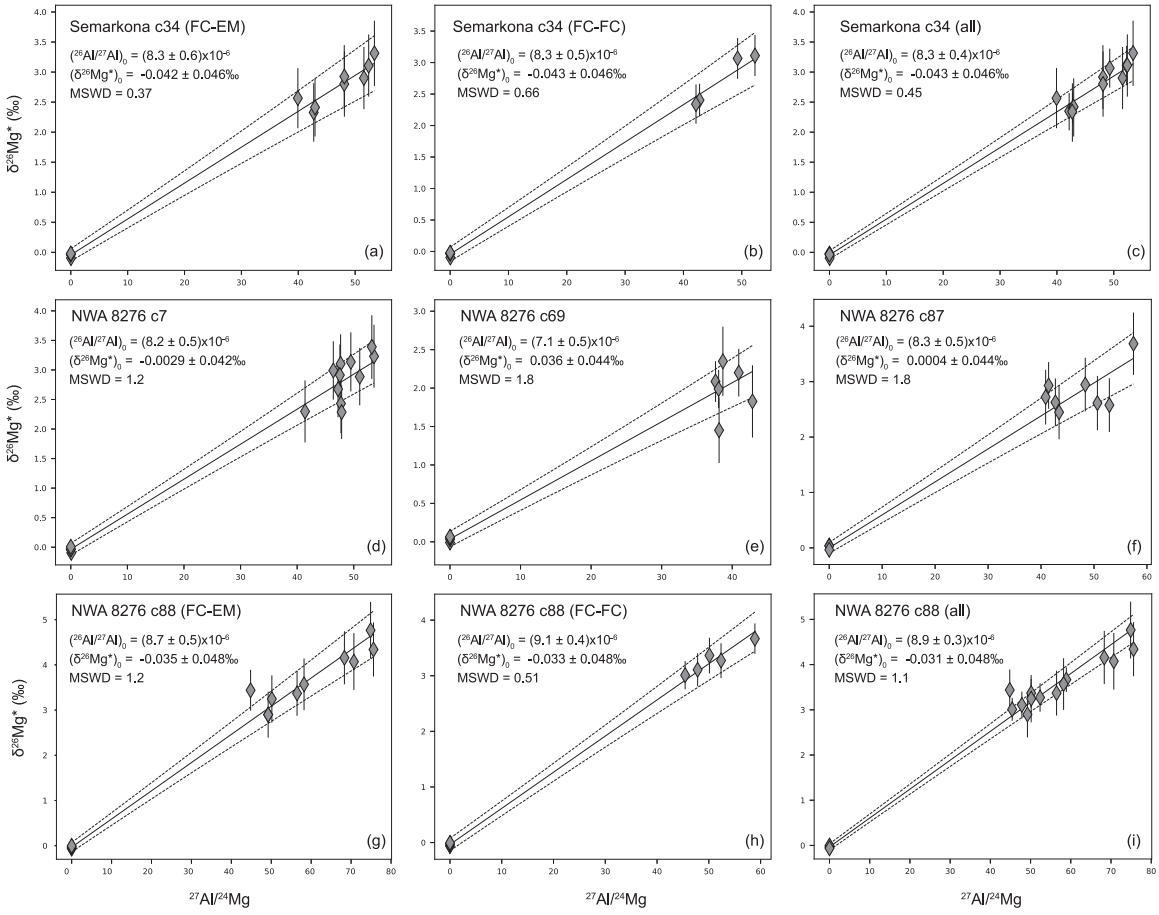

Fig. 10. Internal isochron regression for 5 studied chondrules in this study, including two that were analyzed for MCFC (FC-FC) and FC-EM modes. Error bars represent 2SE. The solid lines represent the regressions and dash lines are 95% confidence interval on the fit. Uncertainties for $(^{26}Al/^{27}Al)_0$ and $(\delta^{26}Mg^*)_0$ are 95% confidence level.

(3.00–3.05), they most probably never experienced temperature above 500 °C (Kimura et al., 2008) and resetting their ^{26}Al-^{26}Mg age by one half-life would take several millions of years for the biggest plagioclase grains. Since all ages exhibit a restricted range, and that at least the Semarkona chondrules and the biggest plagioclase grains cannot realistically be reset by Mg diffusion, it is very unlikely that the majority of Al-Mg isotope systematics presented in this study have been reset during parent body metamorphism.

4.3. Timing of anorthite-bearing chondrule formation

Fig. 11 show the range of $(^{26}Al/^{27}Al)_0$ of the chondrules, from $(6.3 \pm 0.7) \times 10^{-6}$ to $(8.9 \pm 0.3) \times 10^{-6}$. This corresponds to a range of ages comprised between 1.80 ± 0.04 Ma to 2.16 ± 0.11 Ma after CAIs. The kernel distribution shows a major peak at ~1.9 Ma that extend to 2.2 Ma (Fig. 11b). The range is consistent with anorthite-bearing chondrule data from L/LL 3.00–3.15 chondrites with inferred $(^{26}Al/^{27}Al)_0$ of 7×10^{-6} to 1.0×10^{-5} with uncertainties typically from $(1–5) \times 10^{-6}$ (Hutcheon and Hutchison, 1989; Kita et al., 2000, revision by Kita et al., 2010; Mostefaoui et al., 2002; Rudraswami and Goswami, 2007; Bollard et al., 2019). Only 2 out of 11 chondrules are outside of the range observed in this study; QUE 97,008 (L3.05) CH#1B with $(1.95 \pm 0.76) \times 10^{-5}$ (Rudraswami and Goswami, 2007) and NWA 5697 (L3.10) 5-C10 with $(4.4 \pm 1.1) \times 10^{-6}$ (Bollard et al., 2019). In addition Semarkona (LL3.00) type I chondrule CH3 containing fine-grained anorthite show $(^{26}Al/^{27}Al)_0$ of $(7.2 \pm 2.5) \times 10^{-6}$ (Kita et al., 2000, revision by Kita et al., 2010), which is within the same range observed from other chondrules.

The ages determined from the six chondrules from LL chondrites presented here are indistinguishable (1.9 ± 0.1 Ma after CAI formation). In contrast, 8 chondrules in L chondrites show resolvable ages from 1.8 Ma to 2.2 Ma after CAI formation. The uncertainties in the relative ages obtained from this study are mostly between 0.04 Ma and 0.10 Ma, which are smaller than those of previous studies (e.g., Kita et al., 2000; Rudraswami and Goswami, 2007; Rudraswami et al., 2008; Bollard et al., 2019). The fact that both chondrules analyzed with MCFC and FC-EM methods gave indistinguishable ages within errors of 0.04–0.07 Ma is a strong evidence that these uncertainties are not underestimated. Inside this short

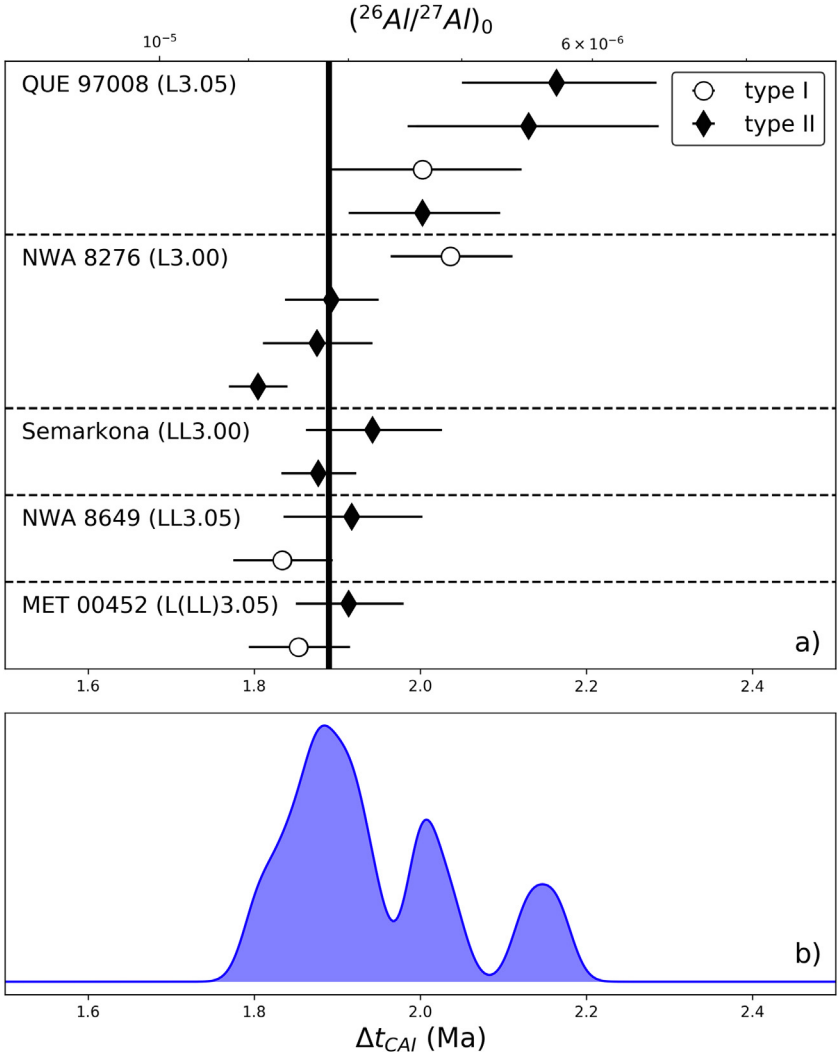

Fig. 11. (a) Compilation of initial $^{26}Al/^{27}Al$ ratios (upper axis) and corresponding age after CAI (lower axis) computed from internal isochron for each chondrule from this study. Error bars shown are uncertainties from isochron regression in Figs. 10 and 11. Chondrule type are as follows: type-I (open dots) and type-II (filled diamonds). The thick black line represents the weighted mean age for all chondrules. (b) Kernel density function for the distribution of all ages from this study.

timescale of 0.4 Ma, there seems to be at least two different chondrule forming events, with two chondrules from QUE 97008 (c143, c150) at 2.13 and 2.16 Ma and the rest being older. The high MSWD for this degree of freedom (MSWD = 1.98, n = 14) for the weighted mean age for all chondrules is also a good indication that there is more than one population of ages. The hypothesis that the two chondrules belong to the same population than the rest of chondrules return a welsh t-test p-value that is extremely low (i.e., 0.0002). Similarly, when taking three different populations, roughly representing the 3 peaks, of <1.95, 1.95–2.05 and >2.05 Ma, all welsh t-test return p-values well below 0.05. When considered separately, these three populations give weighted mean age of 1.86 ± 0.04 Ma (2SD, n = 9, MSWD = 0.77), 2.02 ± 0.10 Ma (2SD, n = 3, MSWD = 0.08), and 2.15 ± 0.18 Ma (2SD, n = 2, MSWD = 0.03), respectively. These three different populations can be seen very easily on the kernel density function of Fig. 11b. Alternatively, these two youngest chondrules in QUE 97008 (c143, c150) could have been affected by parent body metamorphism. They both show the relatively lower $\delta^{26}Mg^*$ values from data with highest $^{27}Al/^{24}Mg$ ratios, which could have been caused by loss of excess ^{26}Mg by diffusion. The younger chondrules in L seems to correspond to the potential second and third populations at 2.0 Ma and 2.15 Ma described above, which need further targeted studies to confirm because only a few chondrules were analyzed in each population. Nevertheless, the small number of data points for each peak is a detriment to any robust statistical analysis that should be completed with more data.

The relationship between type I and II chondrules has been a subject of debate for decades (Jones, 1990; Villeneuve et al., 2015). Recently, oxidation of type I chondrules has been proposed as a mechanism for type II

chondrule formation (Villeneuve et al., 2015). Such a mechanism would imply that type II chondrules are younger than type I. Although only four type I chondrules were measured in this study, this is not what is observed here; type I chondrules show indistinguishable ages from type II chondrules. In Acfer 094 (ungroup C3.00) and the CO3 chondrite Y-81020, type II chondrules show systematically ^{16}O-poor O isotope ratios, compared to type-Is, and frequently contain ^{16}O-rich forsteritic relict grains (Kunihiro et al., 2004, 2005; Ushikubo et al., 2012; Tenner et al., 2013). There are hints of younger Al-Mg ages for type II chondrules than type I chondrules (Kurahashi et al., 2008), which would at least be consistent with the hypothesis. In contrast, types I and II plagioclase-bearing chondrules do not show systematic changes in Δ^{17}O with Mg# (Fig. 8b). They were likely formed in the same chondrule forming environments as typical chondrules, but with different dust-enrichment factors and/or bulk Fe contents that resulted in variable Mg#. The oxidation of type-I chondrule to form type-II chondrule might also happen in a shorter timescale than the precision of the Al-Mg ages from this study. This preclude any definitive conclusion on the process of type-II formation using only Al-Mg ages.

4.4. Comparison to U-Pb ages

Connelly et al. (2012) and Bollard et al. (2017) determined Pb-Pb ages of 13 chondrules from NWA 5697 (L3.10) chondrite, which show ages between 4567.6 Ma to 4563.6 Ma with uncertainties of 0.3–0.7 Ma. Most chondrules studied by Bollard et al. (2017) contained anorthite, indicating that they could have been similar to anorthite-bearing chondrules studied here. Compared to U isotope corrected Pb-Pb ages of CAIs (4567.30 ± 0.13 Ma), these data indicate that formation of L chondrite chondrules started contemporaneously to CAI formation and continued for 4 Ma, in contrast to a narrow range of Al-Mg ages determined in this study. Bollard et al. (2017) suggested that Pb-Pb ages of chondrules represent the time of last chondrule melting because they found that U and radiogenic Pb locate in fine-grained mesostasis phases in chondrules according to SIMS analyses. Therefore, Pb-Pb and Al-Mg systems are supposed to show consistent ages. Bollard et al. (2019) further obtained SIMS Al-Mg analyses of 7 chondrules in NWA 5697 with known Pb-Pb ages along with bulk Al-Mg measurements using high precision solution ICP-MS. As mentioned earlier, the initial (^{26}Al/^{27}Al) ratios determined from isochron regression show values from $(4.5 \pm 1.1) \times 10^{-6}$ to $(8.9 \pm 1.8) \times 10^{-6}$, which are generally consistent with those obtained in this work. In resolving the discrepancy of the ranges of chondrule ages between the two chronometers, Bollard et al. (2019) suggested that ^{26}Al abundance of chondrule precursors were heterogeneous that correlate with the absolute ages.

Alternatively, the Pb-Pb ages of chondrules would be erroneous by regression of Pb-Pb isochron using a series of acid leachates from chondrules. Recently, Blichert-Toft et al. (2020) observed heterogeneous apparent Th/U ratios within and among chondrules in Allende, which were estimated from the analyses of radiogenic ^{208}Pb*/^{206}Pb* ratios and might be related to multiple processes and precursors under variable oxidation state of uranium. They argued that the linear Pb-Pb isotope regression lines from acid leaching could have been a mixing line rather than isochron by reflecting multiple processes or precursors. Furthermore, as observed by Bollard et al. (2017), U and radiogenic Pb locate in mesostasis, because U distribute in chondrule melt rather than olivine and low-Ca pyroxene phenocrysts. Therefore, radiogenic Pb isotope in chondrules would not be easily isolated as acid residues, in contrast to coarse grained CAIs and igneous meteorites that contain Ca-rich pyroxene as a major host of U and radiogenic Pb isotopes. The Cr_2O_3 contents of chondrule olivine in NWA 5697 reported by Bollard et al. (2017) vary from 0.1% to 0.5%, which are more variable and systematically lower than those reported from chondrules in this study (Fig. 4). Such variability in Cr is consistent with higher subtype 3.10 of NWA 5697 than the chondrites used in this work (3.00–3.05). U-Pb system of fine-grained mesostasis would be likely disturbed during mild parent body thermal metamorphism, during which Cr redistribute within olivine. Under such circumstances, Pb-Pb ages of chondrules would become younger if mesostasis lost radiogenic Pb. Altered mesostasis in chondrules could also gain radiogenic Pb that had been released from other U-bearing phases and incorporate more ^{207}Pb due to shorter half-life of ^{235}U, which would result in older Pb-Pb ages. In this regard, the Pb-Pb age of chondrule C3 from NWA 5697 that show highest μ value (^{238}U/^{204}Pb ratio) would be more reliable than those of other chondrules with lower μ values. The Pb-Pb age of C3 is 4566.02 ± 0.26 Ma, which is 2.65 ± 0.36 Ma younger than that of D'Orbigny angrite (4563.37 ± 0.25 Ma; Brennecka and Wadhwa, 2012). The inferred initial (^{26}Al/^{27}Al) ratios of NWA 5697 chondrule C3 and D'Orbigny angrite are $(8.12 \pm 2.76) \times 10^{-6}$ and $(5.06 \pm 0.92) \times 10^{-7}$, respectively, which translate to the time difference of 2.82 ± 0.33 Ma. It is likely that age mismatch between Pb-Pb and Al-Mg chronometers in part due to a choice of age anchor between absolute and relative ages.

4.5. Timing of UOC chondrule formation

The chondrules dated here are all alkali-poor chondrules that are not typical for OC chondrules, though the $(^{26}Al/^{27}Al)_0$ observed from alkali-rich chondrules in the least metamorphosed chondrites (3.00–3.05) in literature generally show a similar range. Kita et al. (2000) reported three type II chondrules with glassy mesostasis or Na-rich plagioclase in Semarkona (LL3.00) and obtained inferred $(^{26}Al/^{27}Al)_0$ from $(4.7 \pm 2.2) \times 10^{-6}$ to $(9.0 \pm 1.6) \times 10^{-6}$. This translate into ages of $1.79 \pm (^{+0.20}/_{-0.17})$ Ma and $2.5 \pm (^{+0.6}/_{-0.4})$ Ma after CAIs. Analyses of six chondrules in LEW 86134 (L3.00) and QUE 97008 (L3.05) by Rudraswami and Goswami (2007) are at relatively large uncertainties, though all chondrules show $(^{26}Al/^{27}Al)_0$ that are within the range observed from anorthite-bearing chondrules in this study, except for one chondrule in LEW 86134 with upper limit of $(^{26}Al/^{27}Al)_0 < 5.3 \times 10^{-6}$. Rudraswami et al. (2008) obtained inferred $(^{26}Al/^{27}Al)_0$ from $(1.10 \pm 0.24) \times 10^{-5}$ to $(5.5 \pm 0.3) \times 10^{-6}$ in the 4

chondrules from Semarkona (LL3.00), all within the range observed in this study. This translate into ages after CAIs of 1.59 $\pm$ ($^{+0.25}/_{-0.20}$) Ma and 2.29 $\pm$ 0.06 Ma. Villeneuve et al. (2009) obtained inferred $(^{26}Al/^{27}Al)_0$ from $(1.62 \pm 0.17) \times 10^{-5}$ to $(3.0 \pm 1.2) \times 10^{-6}$ from 14 chondrules in Semarkona (LL3.00) with a peak at $\sim 7 \times 10^{-6}$, corresponding to the relative ages from 1.20 $\pm$ ($^{+0.11}/_{-0.10}$) Ma to 2.90 ($^{+0.54}/_{-0.35}$) Ma with a peak at 2.0 Ma after CAIs. Pape et al. (2019) obtained inferred $(^{26}Al/^{27}Al)_0$ from $(9.5 \pm 2.8) \times 10^{-6}$ to $(3.1 \pm 1.2) \times 10^{-6}$ from 30 UOC (L/LL 3.00–3.15) chondrules (except for one with only upper limit of 2.6×10^{-6} in NWA 8276 Ch2), corresponding to relative ages from 1.7 $\pm$ 0.3 Ma to 2.9 ($^{+0.5}/_{-0.3}$) Ma after CAIs. This dataset shows a peak of $(^{26}Al/^{27}Al)_0$ at $\sim 5.5 \times 10^{-6}$ and $\sim 7.5 \times 10^{-6}$, corresponding to ages 2.3 Ma and 2.0 Ma after CAIs. Bollard et al. (2019) analyzed two chondrules with glassy mesostasis in NWA 5697 (L3.10), C1 and C2, show $(^{26}Al/^{27}Al)_0$ of $(8.2 \pm 1.0) \times 10^{-6}$ and $(8.1 \pm 2.8) \times 10^{-6}$, respectively, which exactly match the main peak of the distribution obtained in this study.

Villeneuve et al. (2009) and Pape et al. (2019) collected data from typical porphyritic chondrules with glassy mesostasis in UOCs using high precision MCFC analyses that resulted in smaller uncertainties for inferred $(^{26}Al/^{27}Al)_0$ than those of earlier studies using a single collector EM (Kita et al., 2000; Rudraswami and Goswami, 2007; Rudraswami et al., 2008). Thus, they are suitable dataset to compared Al-Mg ages between Na-depleted anorthite-bearing chondrules in this study and normal Na-rich chondrules in UOCs. Their results indicated a peak at 2.0 Ma, which is generally consistent with our results, though they show a broader age distribution that include many chondrules with ages 2.3 Ma or younger. In total 44 chondrules in L/LL 3.00–3.05 UOCs studied by Villeneuve et al. (2009) and Pape et al. (2019), 8 chondrules show inferred $(^{26}Al/^{27}Al)_0$ that are outside of observed range of this study beyond analytical uncertainties; 2 chondrule are higher and 6 are lower including one that only show the upper limit. The discrepancy of age distribution between anorthite-bearing chondrules and normal chondrules in UOCs would be related to different formation environments and timing between two suites of chondrules that show distinct chemical natures. Here we focused on alkali-poor chondrules which are unusual in UOCs, while Villeneuve et al. (2009) and Pape et al. (2019) analyzed a much wider range of chondrule types and mesostasis compositions. Alkali-poor chondrule might have formed at a different time in the solar nebula and during a much more restricted timescale.

Alternatively, large spot analyses employed by Villeneuve et al. (2009) and Pape et al. (2019) could have been affected by parent body metamorphism and/or alterations. Even in Semarkona (3.00), aqueous alteration at low temperatures resulted in minor occurrence of clay minerals in chondrule mesostasis (Grossman et al., 2000; Lewis et al., 2019). SIMS analyses that overlap multiple phases may result in disturbed Al-Mg isochron by including such altered grain boundaries where radiogenic ^{26}Mg could have been lost. The isochron regressions of some chondrules determined by Villeneuve et al. (2009) and Pape et al. (2019) show a significantly large scatter with high MSWD values of 4–5, which were never observed in this study ($\leq$2). Recently, the potential bias of data from regressions with high MSWD has been highlighted for initial $^{10}Be/^{9}Be$ ratios (Dunham et al., 2020). A similar, high precision SIMS analyses by targeting clean Na-rich plagioclase in more typical Na-rich chondrules form UOCs is required to further clarify the entire Al-Mg age distribution of UOCs with the new capabilities offered from the new RF ion source.

Alexander et al. (2008) and Alexander and Ebel (2012) argued that ordinary chondrite chondrules formed in extremely dense environments, which could have had sufficient self-gravity to collapse spontaneously (Alexander et al., 2008), so that UOC chondrules from a single group should show a very narrow formation period, likely <0.1 Ma. By taking only the oldest population of chondrules (1.86 $\pm$ 0.04 Ma), our data may support their hypothesis. However, taking all data in Fig. 11, we do find resolvable ages among chondrules that range from 1.8 Ma to 2.2 Ma. Including other literature data from normal chondrules in UOCs (e.g., Villeneuve et al., 2009; Pape et al., 2019), the total range of chondrule ages are even larger. It is possible that anorthite-bearing chondrules formed earlier in a dust-rich environment, but not as dense as indicated by Alexander et al. (2008). As discussed earlier, the Al-Mg ages of Na-rich porphyritic chondrules (Villeneuve et al., 2009; Pape et al., 2019) may not be significantly different from those of the anorthite-bearing chondrules in this study. Therefore, Na-rich chondrule formation under extreme dust-enrichment might have postdated the formation of the majority of anorthite bearing chondrules at 1.9 $\pm$ 0.1 Ma, formed during the first event, and might have been concurrent with the formation of the younger anorthite-bearing chondrules at 2.0 Ma to 2.15 Ma. It is interesting to note that youngest ages reported in this study are similar to the age estimated for parent body accretion in several studies (Sugiura and Fujiya, 2014; Blackburn et al., 2017), in which abundance of ^{26}Al at the time of accretion is one of the important parameters to determine thermal evolution of the asteroidal bodies. Blackburn et al. (2017) estimated the accretion time of H and L chondrites to be from 2.05 Ma to 2.25 Ma after CAIs. UOC chondrule ages that are significantly younger than 2.3 Ma after CAIs may not be consistent with the timing of parent body formation expected from thermal model. Future study may focus on determination of youngest chondrules in UOC and careful evaluation of the extents of parent body metamorphism on the Al-Mg system.

5. CONCLUSION

In this study we determined the $(^{27}Al/^{26}Al)_0$ of 14 anorthite bearing chondrules from 5 different unequilibrated ordinary chondrites (UOCs), with a wide range of chondrule types and compositions. New analytical development using a multi-collection FC-EM detector configuration allows for the precise measurements of excess ^{26}Mg in plagioclase at the level of $\pm$0.5–0.7‰ from a single 6 μm SIMS spot analyses. Multi-collection FC (MCFC) analyses with a

spot size of ~15 μm allow for 0.3–0.4‰ uncertainty. These improved analytical precisions allow us to determine Al-Mg ages of chondrules with precisions better than 0.1 Ma. We conclude the following:

1) Anorthite bearing chondrules show a wide range of Mg# and textural relationships between olivine/pyroxene and anorthites. Some show mineral and compositional zoning indicative of crystallization from the rim inwards, suggesting that they are not fragments of former differentiated objects, but instead a minor group of chondrules uniquely found in L and LL chondrites. Anorthite in these chondrules show silica excess and relatively high MgO contents, indicating that they preserved their primary high temperature characteristics.
2) All chondrules show resolvable $\delta^{26}Mg^*$ and yield Al-Mg isochrons with acceptable MSWD. Their $(^{27}Al/^{26}Al)_0$ range from $(6.3 \pm 0.4) \times 10^{-6}$ to $(8.9 \pm 0.2) \times 10^{-6}$. Assuming a homogeneous distribution of ^{26}Al in the Solar System with a canonical $(^{27}Al/^{26}Al)_0$ value of 5.25×10^{-5} at the time of CAI formation, these chondrule formed from 1.80 ± 0.04 to 2.16 ± 0.11 Ma after CAIs.
3) The formation ages of anorthite-bearing chondrules are at the peak of those of normal Na-rich chondrules, though the timescale for chondrule formation reported in this study of < 0.4 Ma is much shorter than those estimated by Villeneuve et al. (2009) and Pape et al. (2019). The youngest age observed from this study is consistent with the estimated time of accretion of ordinary chondrite parent bodies (e.g., Blackburn et al., 2017).
4) Resolvable ages among chondrules in this study indicate that chondrules did not form during a single event, but potentially 2 or 3 discrete chondrule forming events. These different events might not have been coeval for L and LL chondrites since all younger ages are found for chondrules in L chondrites. This is not consistent with the very short duration (<0.1 Ma) expected from extremely dense chondrule forming environments, which might not be applied to Na-depleted anorthite bearing chondrules in this study.

Declaration of Competing Interest

The authors declare that they have no known competing financial interests or personal relationships that could have appeared to influence the work reported in this paper.

ACKNOWLEDGMENTS

We thank Steve Simon, Timothy McCoy, and ANSMET program for allocation of meteorite samples. We acknowledge extensive supports from John Fournelle for EPMA, and Bill Schneider for SEM, and Michael Spicuzza for SIMS. Michael Spicuzza reviewed an earlier version of this manuscript. Constructive reviews were provided by Conel Alexander, anonymous reviewers, and associate editor Anders Meibom, which improved the quality of the manuscript. This work is supported by NASA Emerging World Program (NNX17AE29G, N. K.). The upgrade of the RF plasma ion source is supported by the NASA Laboratory Analysis of Returned Samples and Planetary Major Equipment Programs (NNX16AG80G) and the NSF Instrumentation and Facility Program (EAR-1355590). WiscSIMS is partly supported by NSF (EAR-1658823). FIB instrumentation was supported by NSF through the University of Wisconsin Materials Research Science and Engineering Center (DMR-17204015).

APPENDIX A. SUPPLEMENTARY MATERIAL

Supplementary data to this article can be found online at https://doi.org/10.1016/j.gca.2020.10.025.

REFERENCES

Alexander C. M. O. (2005) From supernovae to planets: the view from meteorites and interplanetary dust particles. In ASP Conference Series (eds. A. N. Krot and E. R. D. Scott), pp. 972–1002.

Alexander C. M. O. and Ebel D. S. (2012) Questions, questions: can the contradictions between the petrologic, isotopic, thermodynamic, and astrophysical constraints on chondrule formation be resolved? *Meteorit. Planet. Sci.* **47**, 1157–1175.

Alexander C. M. O., Barber D. J. and Hutchison R. (1989) The microstructure of Semarkona and Bishunpur. *Geochim. Cosmochim. Acta* **53**, 3045–3057.

Alexander C. M. O., Grossman J. N., Ebel D. S. and Ciesla F. J. (2008) The formation conditions of chondrules and chondrites. *Science* **320**, 1617–1619.

Anon. (2014) Comment on Bybee et al. (2014): Pyroxene megacrysts in Proterozoic anorthosites: implications for tectonic setting, magma source and magmatic processes at the Moho. Earth Planet. Sci. Lett. 401, 378–380.

Beaty D. W. and Albee A. L. (1980) Silica solid solution and zoning in natural plagioclase. *Am. Mineral.* **65**, 63–74.

Berlin J., Jones R. H. and Brearley A. J. (2011) Fe-Mn systematics of type IIA chondrules in unequilibrated CO, CR, and ordinary chondrites. *Meteorit. Planet. Sci.* **46**, 513–533.

Blackburn T., Alexander C. M. O., Carlson R. and Elkins-Tanton L. T. (2017) The accretion and impact history of the ordinary chondrite parent bodies. *Geochim. Cosmochim. Acta* **200**, 201–217.

Blichert-Toft J., Göpel C., Chaussidon M. and Albarède F. (2020) Th/U variability in Allende chondrules. *Geochim. Cosmochim. Acta* **280**, 378–394.

Bollard J., Connelly J. N., Whitehouse M. J., Pringle E. A., Bonal L., Jørgensen J. K., Nordlund Å., Moynier F. and Bizzarro M. (2017) Early formation of planetary building blocks inferred from Pb isotopic ages of chondrules. *Sci. Adv.* **3**, 1–10.

Bollard J., Kawasaki N., Sakamoto N., Olsen M., Itoh S., Larsen K., Wielandt D., Schiller M., Connelly J. N., Yurimoto H. and Bizzarro M. (2019) Combined U-corrected Pb-Pb dating and 26Al-26Mg systematics of individual chondrules – evidence for a reduced initial abundance of 26Al amongst inner Solar System chondrules. *Geochim. Cosmochim. Acta* **260**, 62–83.

Bruno E. and Facchinelli A. (1975) Crystal-chemical interpretation of crystallographic anomalies in lunar plagioclases. *bulmi* **98**, 113–117.

Brennecka G. A. and Wadhwa M. (2012) Uranium isotope compositions of the basaltic angrite meteorites and the chronological implications for the early Solar System. *PNAS* **109**, 9299–9303.

Budde G., Kruijer T. S. and Kleine T. (2018) Hf-W chronology of CR chondrites: implications for the timescales of chondrule

formation and the distribution of 26Al in the solar nebula. *Geochim. Cosmochim. Acta* **222**, 284–304.
Catanzaro E. J., Murphy T. J., Garner E. L. and Shields W. R. (1966) Absolute isotopic abundance ratios and atomic weight of magnesium. *J. Res. Nat. Bur. Stand.* **70A**, 453–458.
Clayton R. N., Mayeda T. K., Goswami J. N. and Olsen E. J. (1991) Oxygen isotope studies of ordinary chondrites. *Geochim. Cosmochim. Acta* **55**, 2317–2337.
Connelly J. N., Bizzarro M., Krot A. N., Nordlund A., Wielandt D. and Ivanova M. A. (2012) The absolute chronology and thermal processing of solids in the solar protoplanetary disk. *Science* **338**, 651–655.
Cuzzi J. N., Hogan R. C. and Bottke W. F. (2010) Towards initial mass functions for asteroids and Kuiper Belt Objects. *Icarus* **208**, 518–538.
Davis A. M., Richter F. M., Mendybaev R. A., Janney P. E., Wadhwa M. and McKeegan K. D. (2015) Isotopic mass fractionation laws for magnesium and their effects on 26Al–26Mg systematics in solar system materials. *Geochim. Cosmochim. Acta* **158**, 245–261.
Desch S. J., Morris M. A., Connolly, Jr, H. C. and Boss A. P. (2012) The importance of experiments: constraints on chondrule formation models. *Meteorit. Planet. Sci.* **47**, 1139–1156.
Donovan J. J., Singer J. W. and Armstrong J. T. (2016) A new EPMA method for fast trace element analysis in simple matrices. *Am. Mineral.* **101**, 1839–1853.
Dunham E. T., Wadhwa M., Desch S. J. and Hervig R. L. (2020) Best practices for determination of initial 10Be/9Be in early solar system materials by secondary ion mass spectrometry. *Geostand. Geoanal. Res.* **52**, 1–16.
Ebel D. S. and Grossman L. (2000) Condensation in dust-enriched system. *Geochimica et Cosmochimica Acta* **64**, 339–366.
Fukuda K., Brownlee D. E., Joswiak D. J., Tenner T. J., Kimura M. and Kita N. T. (2020a) Correlated isotopic and chemical evidence for condensation origins of olivine in comet 81P/Wild 2 and in AOAs from CV and CO chondrites. *Geochim. Cosmochim. Acta*, 1–65.
Fukuda K., Beard B. L., Dunlap D. R., Spicuzza M. J., Fournelle J. H., Wadhwa M. and Kita N. T. (2020b) Magnesium isotope analysis of olivine and pyroxene by SIMS: evaluation of matrix effects. *Chem. Geol.* **540**, 119482.
Grossman J. N. (1988) Chondrites and the solar nebula. *Nature* **334**, 14–15.
Grossman J. N., Alexander C. M. O., Wang J. and Brearley A. J. (2000) Bleached chondrules: Evidence for widespread aqueous processes on the parent asteroids of ordinary chondrites. *Meteoritics and Planetary Science* **35**, 467–486.
Grossman J. N. and Brearley A. J. (2005) The onset of metamorphism in ordinary and carbonaceous chondrites. *Meteorit. Planet. Sci.* **40**, 87–122.
Hertwig A. T., Kimura M., Ushikubo T., Defouilloy C. and Kita N. T. (2019) The 26Al-26Mg systematics of FeO-rich chondrules from Acfer 094: Two chondrule generations distinct in age and oxygen isotope ratios. *Geochim. Cosmochim. Acta* **253**, 111–126.
Hutcheon I. D. and Hutchison R. (1989) Evidence from the Semarkona ordinary chondrite for 26Al heating of small planets. *Lett. Nat.* **337**, 238–241.
Hutcheon I. D. and Jones R. H. (1995) The 26Al-26Mg record of chondrules: clues to nebular chronology. *Lunar Planet. Sci.* **25**, 587–588.
Isa J., Kohl I. E., Liu M. C., Wasson J. T., Young E. D. and McKeegan K. D. (2017) Quantification of oxygen isotope SIMS matrix effects in olivine samples: correlation with sputter rate. *Chem. Geol.* **458**, 14–21.
Jacobsen B., Yin Q.-Z., Moynier F., Amelin Y., Krot A. N., Nagashima K., Hutcheon I. D. and Palme H. (2008) 26Al–26Mg and 207Pb–206Pb systematics of Allende CAIs: canonical solar initial 26Al/27Al ratio reinstated. *Earth Planet. Sci. Lett.* **272**, 353–364.
Jones R. H. (1990) Petrology and mineralogy of Type II, FeO-rich chondrules in Semarkona (LL3.0): origin by closed-system fractional crystallization, with evidence for supercooling. *Geochim. Cosmochim. Acta* **54**, 1785–1802.
Jones R. H. (1994) Petrology of FeO-poor, porphyritic pyroxene chondrules in the Semarkona chondrite. *Geochim. Cosmochim. Acta* **58**, 5325–5340.
Jones R. H. (2012) Petrographic constraints on the diversity of chondrule reservoirs in the protoplanetary disk. *Meteorit. Planet. Sci.* **47**, 1176–1190.
Kimura M., Grossman J. N. and Weisberg M. K. (2008) Fe-Ni metal in primitive chondrites: indicators of classification and metamorphic conditions for ordinary and CO chondrites. *Meteorit. Planet. Sci.* **43**, 1161–1177.
Kita N. T. and Ushikubo T. (2012) Evolution of protoplanetary disk inferred from 26Al chronology of individual chondrules. *Meteorit. Planet. Sci.* **47**, 1108–1119.
Kita N. T., Nagahara H., Togashi S. and Morishita Y. (2000) A short duration of chondrule formation in the solar nebula: evidence from 26Al in Semarkona ferromagnsian chondrules. *Geochim. Cosmochim. Acta* **64**, 3913–3922.
Kita N. T., Ushikubo T., Fu B. and Valley J. W. (2009) High precision SIMS oxygen isotope analysis and the effect of sample topography. *Chem. Geol.* **264**, 43–57.
Kita N. T., Nagahara H., Tachibana S., Tomomura S., Spicuzza M. J., Fournelle J. H. and Valley J. W. (2010) High precision SIMS oxygen three isotope study of chondrules in LL3 chondrites: role of ambient gas during chondrule formation. *Geochim. Cosmochim. Acta* **74**, 6610–6635.
Kita N. T., Ushikubo T., Knight K. B., Mendybaev R. A., Davis A. M., Richter F. M. and Fournelle J. H. (2012) Internal ^{26}Al-^{26}Mg isotope systematics of a Type B CAI: Remelting of refractory precursor solids. *Geochim. Cosmochim. Acta* **86**, 37–51.
Kita N. T., Yin Q.-Z., MacPherson G. J., Ushikubo T., Jacobsen B., Nagashima K., Kurahashi E., Krot A. N. and Jacobsen S. B. (2013) 26Al- 26Mg isotope systematics of the first solids in the early solar system. *Meteorit. Planet. Sci.* **48**, 1383–1400.
Kita N. T., Hertwig A. T., Defouilloy C., Kitajima K. and Spicuzza M. J. (2018) Improvements of SIMS Mg isotope analyses for meteoritic and cometary samples using RF plasma ion source. In 50th Lunar and Planetary Science Conference. #2441.
Kita N. T., Siron G. and Kimura M. (2019) Petrographic examination of unequilibrated ordinary chondrites with low petrologic subtypes. metsoc. #6237.
Kunihiro Takuy, Rubin A. E., McKeegan K. D. and Wasson J. T. (2004) Oxygen-isotopic compositions of relict and host grains in chondrules in the Yamato 81020 CO3.0. *Geochim. Cosmochim. Acta* **68**, 3599–3606.
Kunihiro Ta, Rubin A. E. and Wasson J. T. (2005) Oxygen-isotopic compositions of low-FeO relicts in high-FeO host chondrules in Acfer 094, a type 3.0 carbonaceous chondrite closely related to CM. *Geochim. Cosmochim. Acta* **69**, 3831–3840.
Kurahashi E., Kita N. T., Nagahara H. and Morishita Y. (2008) ^{26}Al–^{26}Mg systematics of chondrules in a primitive CO chondrite. *Geochim. Cosmochim. Acta* **72**, 3865–3882.
Larsen K. K., Trinquier A., Paton C., Schiller M., Wielandt D., Ivanova M. A., Connelly J. N., Nordlund Å., Krot A. N. and

Bizzarro () Evidence for magnesium isotope heterogeneity in the solar protoplanetary disk. *ApJ* **735**, L37–L47.

Larsen K. K., Schiller M. and Bizzarro M. (2016) Accretion timescales and style of asteroidal differentiation in an 26Al-poor protoplanetary disk. *Geochim. Cosmochim. Acta* **176**, 295–315.

Lewis J. A. and Jones R. H. (2018) Primary feldspar in the Semarkona LL3.00 chondrite: Constraints on chondrule formation and secondary alteration. *Meteoritics & Planetary Science* **54**, 72–89.

Longhi J. and Hays J. F. (1979) Phase equilibria and solid solution along the join $CaAl_2Si_2O_8$-SiO_2. *Am. J. Sci.* **279**, 876–890.

Longhi J., Walker D. and Hays J. F. (1976) Fe and Mg plagioclase. In Proc. Lunar Sci. Conf. 7th, pp. 1281–1300.

MacPherson G. J. and Huss G. R. (2005) Petrogenesis of Al-rich chondrules: evidence from bulk compositions and phase equilibria. *Geochim. Cosmochim. Acta* **69**, 3099–3127.

Mittlefehldt D. W. and Berger E. L. (2017) Excess silica substitution in plagioclase grains in the Pasamonte eucrite. *Meteorit. Planet. Sci.*, 1.

Mostefaoui S., Kita N. T., Togashi S., Tachibana S., Nagahara H. and Morishita Y. (2002) The relative formation ages of ferromagnesian chondrules inferred from their initial aluminum-26/aluminum-27 ratios. *Meteorit. Planet. Sci.* **37**, 421–438.

Nishiizumi K. (2004) Preparation of 26Al AMS standards. *Nucl. Instrum. Methods Phys. Res., Sect. B* **223–224**, 388–392.

Pape J., Mezger K., Bouvier A. S. and Baumgartner L. P. (2019) Time and duration of chondrule formation: constraints from 26Al-26Mg ages of individual chondrules. *Geochim. Cosmochim. Acta* **244**, 416–436.

Rudraswami N. G. and Goswami J. N. (2007) 26Al in chondrules from unequilibrated L chondrites: Onset and duration of chondrule formation in the early solar system. *Earth Planet. Sci. Lett.* **257**, 231–244.

Rudraswami N. G., Goswami J. N., Chattopadhyay B., Sengupta S. K. and Thapliyal A. P. (2008) 26Al records in chondrules from unequilibrated ordinary chondrites: II. Duration of chondrule formation and parent body thermal metamorphism. *Earth Planet. Sci. Lett.* **274**, 93–102.

Russell S. S., Srinivasan G., Huss G. R., Wasserburg G. J. and MacPherson G. J. (1996) Evidence for widespraed 26Al in the solar Nebula and constraints for Nebula time scales. *Science* **273**, 757–762.

Russell S. S., Huss G. R., MacPherson G. J. and Wasserburg G. J. (1997) Early and late chondrule formation: new contraints for solar nebula chronology from 26Al/27Al in unequilibrated ordinary chondrites. In 28th Lunar and Planetary Science Conference. #1468.

Spear F. S., Rumble, III, D. and Ferry J. M. (1982) Linear algebraic manipulation of n-dimensional composition space. *Rev. Mineral. Geochem.* **10**, 53–104.

Sugiura N. and Fujiya W. (2014) Correlated accretion ages and ε 54Cr of meteorite parent bodies and the evolution of the solar nebula. *Meteorit. Planet. Sci.* **49**, 772–787.

Tachibana S., Nagahara H., Mostefaoui S. and Kita N. T. (2003) Correlation between relative ages inferred from 26Al and bulk compositions of ferromagnesian chondrules in least equilibrated ordinary chondrites. *Meteorit. Planet. Sci.* **38**, 939–962.

Tenner T. J., Ushikubo T., Kurahashi E., Kita N. T. and Nagahara H. (2013) Oxygen isotope systematics of chondrule phenocrysts from the CO3.0 chondrite Yamato 81020: evidence for two distinct oxygen isotope reservoirs. *Geochim. Cosmochim. Acta* **102**, 226–245.

Tenner T. J., Nakashima D., Ushikubo T., Tomioka N., Kimura M., Weisberg M. K. and Kita N. T. (2019) Extended chondrule formation intervals in distinct physicochemical environments: evidence from Al-Mg isotope systematics of CR chondrite chondrules with unaltered plagioclase. *Geochim. Cosmochim. Acta* **260**, 133–160.

Thompson J. B. (1982) Compositional space: an algebraic and geometric approach. *Rev. Mineral. Geochem.* **10**, 1–32.

Ushikubo T., Kimura M., Kita N. T. and Valley J. W. (2012) Primordial oxygen isotope reservoirs of the solar nebula recorded in chondrules in Acfer 094 carbonaceous chondrite. *Geochim. Cosmochim. Acta* **90**, 242–264.

Ushikubo T., Tenner T. J., Hiyagon H. and Kita N. T. (2017) A long duration of the 16O-rich reservoir in the solar nebula, as recorded in fine-grained refractory inclusions from the least metamorphosed carbonaceous chondrites. *Geochim. Cosmochim. Acta* **201**, 103–122.

Valley J. W. and Kita N. T. (2009) In situ oxygen isotope geochemistry by ion microprobe. *Mineral. Assoc. Canada Short Course* **41**, 19–63.

Van Orman J. A., Cherniak D. J. and Kita N. T. (2014) Magnesium diffusion in plagioclase: dependence on composition, and implications for thermal resetting of the 26Al–26Mg early solar system chronometer. *Earth Planet. Sci. Lett.* **385**, 79–88.

Vermeesch P. (2018) IsoplotR: A free and open toolbox for geochronology. *Geosci. Front.* **9**, 1479–1493.

Villeneuve J., Chaussidon M. and Libourel G. (2009) Homogeneous distribution of 26Al in the solar system from the Mg isotopic composition of chondrules. *Science* **325**, 985–988.

Villeneuve J., Libourel G. and Soulié C. (2015) Relationships between type I and type II chondrules: Implications on chondrule formation processes. *Geochim. Cosmochim. Acta* **160**, 277–305.

Weil D. F., McCallum I. S., Bottinga Y., Drake M. J. and McKay G. A. (1970) Mineralogy and petrology of some Apollo 11 igneous rocks. In *Proceedings of the Apollo Lunar Science Conference*, pp. 937–955.

Wenk H.-R. and Wilde W. R. (1973) Chemical anomalies of lunar plagioclase, described by substitution vectors and their relation to optical and structural properties. *Contrib. Mineral Petrol.* **41**, 89–104.

York D., Evensen N. M., Martı´nez M. L. and De Basabe Delgado J. (2004) Unified equations for the slope, intercept, and standard errors of the best straight line. *Am. J. Phys.* **72**, 367–375.

Associate editor: Anders Meibom